4

Coseismic Damage Generation and Pulverization in Fault Zones: Insights From Dynamic Split-Hopkinson Pressure Bar Experiments

Franciscus M. Aben[1,2], Mai-Linh Doan[1,2], Jean-Pierre Gratier[1,2], and François Renard[1,2,3]

ABSTRACT

Coseismic damage in fault zones contributes to the short- and long-term behavior of a fault and provides a valuable indication of the parameters that control seismic ruptures. This review focuses on the most extreme type of off-fault coseismic damage: pulverized rock. Such pervasively fractured rock that does not show any evidence of shear strain is observed mainly along large strike-slip faults. Field observations on pulverized rock are briefly examined and would suggest that dynamic (high strain rate) deformation is responsible for its generation. Therefore, these potential paleo-seismic markers could give an indication of the constraints on rupture propagation conditions. Such constraints can be determined from dynamic loading experiments, typically performed on a Split-Hopkinson Pressure Bar apparatus. The principle of this apparatus is summarized and experimental studies on dynamic loading and pulverization are reviewed. For compressive dynamic loading, these studies reveal a strain rate threshold above which pulverization occurs. The nature of the pulverization threshold is discussed by means of several fracture mechanics models. The experimental pulverization conditions are correlated with field observations by analyzing and discussing several earthquake rupture models. An indisputable rupture mechanism could not be established owing to a gap in experimental knowledge, especially regarding tensile dynamic loading.

4.1. INTRODUCTION

Damage to rock formations surrounding faults can have a major influence on the mechanical behavior of the faults, whether they are seismogenic or aseismically creeping faults. Fracturing may increase, at least temporarily, the permeability of the damaged rock, leading to episodic fluid flow that modifies its rheological properties [*Sibson*, 1996; *Miller*, 2013]. Fracturing may contribute to the development of anisotropy around the fault zone [*Crampin and Booth*, 1985; *Zhao et al.*, 2011] and may also activate chemical reactions facilitating stress-driven mass transfer creep [*Gratier et al.*, 2013b, 2014]. Subsequent sealing of the fractures may strengthen the rock, contributing to mechanical segregation in a fault zone and possibly leading to localized earthquakes [*Li et al.*, 2003; *Zhao et al.*, 2011; *Gratier et al.*, 2013a]. Such a heterogeneity could in turn be a tuning parameter in fault slip and earthquake dynamics [*Bürgmann et al.*, 1994; *Zöller et al.*, 2005].

Conversely, the behavior of the fault itself influences the amount and type of damage occurring in the damage zone [*Faulkner et al.*, 2011]. This damage may be caused by a variety of quasi-static and dynamic deformation processes [*Mitchell and Faulkner*, 2009]. The mutual interaction between fault and damage zone is not yet fully understood, especially the long-term effects, including gradual chemical changes of the fault core gouge that might change the behavior of the fault zone from seismic

[1] *Université Grenoble Alpes, ISTerre, Grenoble, France*
[2] *CNRS, ISTerre, Grenoble, France*
[3] *PGP, Department of Geosciences, University of Oslo, Oslo, Norway*

Fault Zone Dynamic Processes: Evolution of Fault Properties During Seismic Rupture, Geophysical Monograph 227,
First Edition. Edited by Marion Y. Thomas, Thomas M. Mitchell, and Harsha S. Bhat.

to aseismic permanent creep [*Richard et al.*, 2014]. Consequently, damage development processes in faults are a crucial factor in understanding the mechanics of faults.

Within the damage zone, coseismically damaged rock formations provide a means of constraining fault and earthquake mechanics given that they were formed by seismic events. Coseismically damaged rocks differ from other damage zone rocks inasmuch that they are dynamically loaded in tension or compression by stress waves surrounding a propagating rupture tip for a short duration. Due to dynamic loading, the kinetics of fracture propagation controls the damage process [*Grady*, 1998] and not just the local state of stress as is the case for quasi-static crack growth.

The most extreme coseismic end-member is thought to be pulverized rock, and therefore this rock has the highest potential both as a seismic marker and as a process that drastically modifies the mechanical properties of the fault zone. Pulverized rocks are in situ exploded rocks that have been subjected to pervasive fracturing up to the micrometer scale, without any accumulation of shear strain. The fracture damage is mechanical in nature, and this type of rock is almost exclusively present in the top few kilometers along major strike-slip faults. Such rock could potentially be indicative of one or several paleoseismic events. Moreover, these rocks might give constraints on the magnitude, loading conditions, and rupture direction. For the time being, such constraints remain open questions.

Since being acknowledged as a source of information for earthquake events by *Brune* [2001] and *Dor et al.* [2006b], research on these rocks is still in a preliminary phase. A strict definition including more than the qualitative description given above has not yet been established for this type of rock. Furthermore, the factors setting these rocks apart from their lesser coseismically damaged peers in terms of damage process have yet to be defined.

These questions can partly be answered by mapping the processes and conditions in which pulverized rocks can be formed. This also includes studying nonpulverized coseismically damaged rocks to constrain the entire range of fracture damage products that might be expected during a seismic event. To this end, laboratory experiments are crucial whereby samples are exposed to stress wave loading, similar to the high-frequency waves emitted during an earthquake. In contrast to many other physical and mechanical experiments on rocks, a time transformation from laboratory loading rates to natural loading rates is not necessary; rather, the challenge is to simulate the fast loading rates of a seismic rupture.

This review-style chapter starts with a summary of field observations on pulverized rock, including an outline of the issues regarding the definition of a pulverized rock. The current state-of-the-art high loading rate experiments will then be presented, first in general form and second for pulverization in particular. Since these experimental studies are performed mostly on the Split-Hopkinson Pressure Bar apparatus, a short overview of this technique is given. More details are then given of current dynamic fracture models and theories in the high strain rate regime to explain the transition to pulverized rocks. Finally, current experimental knowledge and field observations are linked to earthquake rupture mechanical models, and their implications for fault zones containing pulverized rocks are discussed.

4.2. FIELD OBSERVATIONS OF PULVERIZED ROCK RELATED TO COSEISMIC DAMAGE

4.2.1. Observations, Definition, and Microstructures of Pulverized Rock

The first observations of pulverized rocks were at or near the surface along the San Andreas fault between San Bernardino and Tejon Pass on granites and gneisses [*Brune,* 2001; *Dor et al.,* 2006b]. Prior to this, these rocks might have been overlooked or labeled as gouges and cataclasites after the classic definition [*Sibson*, 1977; *Wilson et al.*, 2005]. However, the features setting them apart from these classic fault zone rocks are well summarized in the field definition given by *Dor et al.* [2006b]: A rock is classified as pulverized when the original textures are preserved (Figure 4.1a), very little or no shear is visible and all the crystals in a sample yield a powdery rock-flour texture when pressed in the hand. This damage is widespread on the outcrop scale. At the field scale, these rocks can be easily recognized due to their badland-type morphology [*Dor et al.*, 2006a, 2006b, 2008; *Mitchell et al.*, 2011] (Figure 4.1b) and faster erosion rate compared with the surrounding rocks.

On a smaller scale, pulverized igneous crystalline rocks (granite, granodiorite, gneiss) are characterized by a large number of fractures seemingly oriented randomly in 3D and without any clear hierarchical organization (Figure 4.1c, d). The fracture density is very high and, in general, the fractures penetrate all mineral phases, although some minerals may contain fewer fractures in places where the rock is less pulverized. Fracture patterns can be either random or follow cleavage planes, and micas can be kinked or contain fewer fractures than other mineral phases (Figure 4.1e). The dilatational mode I fractures show very little offset, and the fragments bounded by the fractures show little to no rotation, as evidenced by cross-polarized images in which original grains can be clearly identified from the myriad of fragments (Figure 4.1f, g). Since weathering might alter granitic

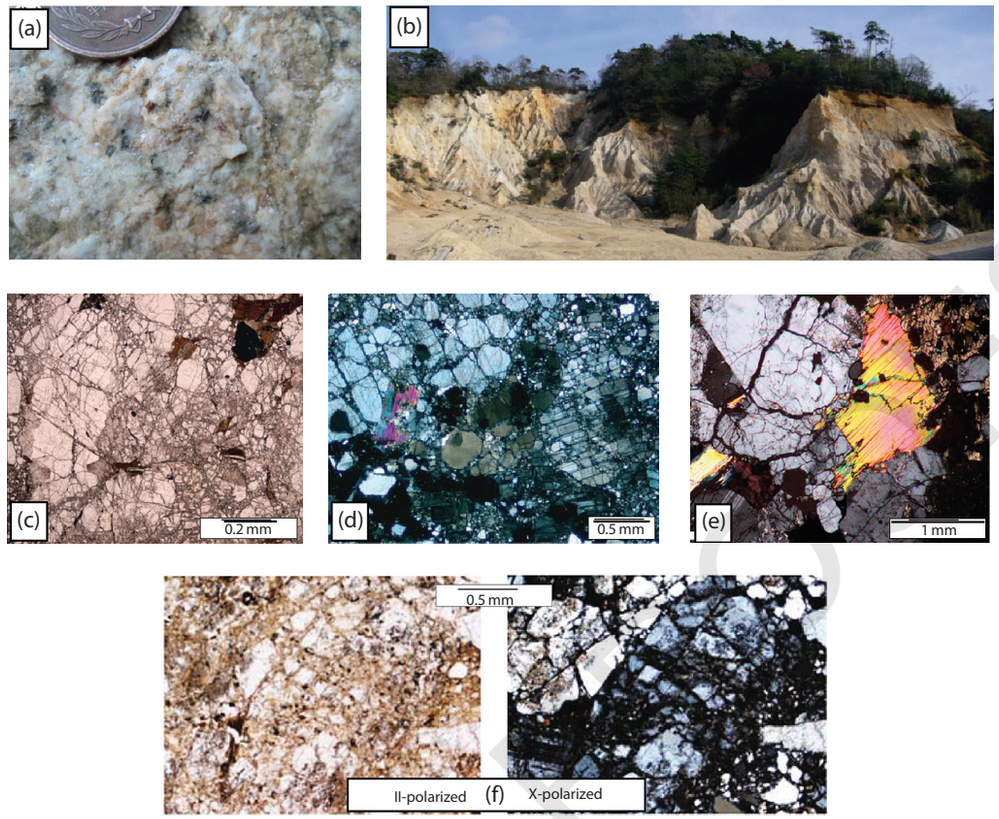

Figure 4.1 (a) Image of a pulverized granite showing a clear pristine crystalline texture. (b) Typical badland erosion geomorphology related to pulverized rocks. (c)–(e) Photomicrographs of pulverized granitic rocks. Image (c) is taken with parallel polarizers, (d) and (e) with crossed polarizers. Image (e) contains a slightly buckled biotite grain. (f) Photomicrographs with parallel (left) and crossed (right) polarizers show that hardly any rotation or movement of fragments has occurred. Sources: (a), (b) *Mitchell et al.* [2011], (c) *Rempe et al.* [2013], (d) *Wechsler et al.* [2011], (e) *Muto et al.* [2015], and (f) *Rockwell et al.* [2009].

rocks toward a more fragile lithology, several authors have conducted mineralogical studies that have ruled out this mechanism [*Rockwell et al.*, 2009; *Mitchell et al.*, 2011; *Wechsler et al.*, 2011] and they have proposed a mechanical origin instead. This, together with the microstructures, indicates a mechanical source for pulverization.

In some studies, geometric analyses have been conducted to characterize crystalline pulverized rocks in greater detail. Particle size distributions (PSD) were obtained on San Andreas pulverized rocks by *Wilson et al.* [2005], *Rockwell et al.* [2009], and *Wechsler et al.* [2011] using a specially calibrated laser particle size analyzer. The results indicated nonfractal PSD behavior toward larger grain sizes (>500 μm). For smaller grain sizes (0.5–500 μm), a *D*-value fractal exponent in the range 2.5–3.1 provided the best power law fit. Moreover, *Wilson et al.* [2005] constrained surface areas of up to 80 m^2/g, although it is not clear whether this was actual gouge or pulverized rock. *Muto et al.* [2015] determined a PSD from thin sections of pulverized rocks taken from the San Andreas fault and the Arima-Takatsuki Tectonic line (Japan). For both locations, fractal dimensions vary from 2.92 close to the fault core to 1.92 at some distance from the fault core, although the latter samples were not labeled as being pulverized. The *D*-values from *Wechsler et al.* [2011] and *Muto et al.* [2015] exceed the fractal dimensions of PSDs measured on experimental and field samples of gouges and cataclasites with a high shear strain component. These rocks give maximum *D*-values of ~2.5 [e.g., *Monzawa and Otsuki*, 2003; *Keulen et al.*, 2007; *Stünitz et al.*, 2010]. Thus, PSDs of igneous crystalline pulverized rock are nonfractal at larger grain sizes, and at a finer fractal grain size range they have higher *D*-values compared to cataclasites and gouges, although this range of *D*-values is nonunique since the lower limits overlap with shear-related fault rocks.

All the "classic" characterizations of pulverized rock presented above were obtained from igneous crystalline

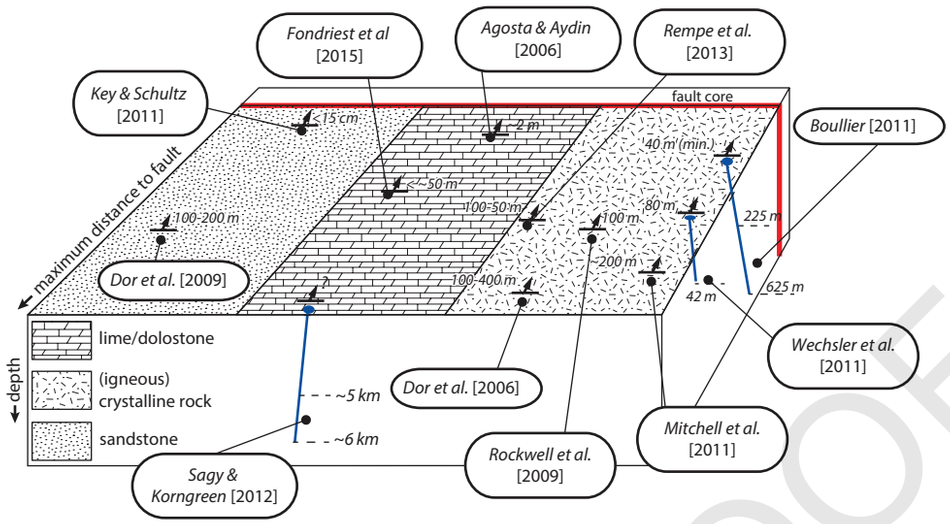

Figure 4.2 Summary of studies on pulverized rocks in the field. The general lithology of the pulverized rock is indicated as well as the in situ location with respect to the fault, including in situ depth of observation (boreholes are indicated in blue). This depth must not be confused with the depth at which the pulverized rocks have been formed. *See electronic version for color representation*.

rock samples (Figure 4.2), taken mostly from along the San Andreas active fault zone and its nonactive strands [*Wilson et al.*, 2005; *Dor et al.*, 2006a, 2006b; *Rockwell et al.*, 2009; *Wechsler et al.*, 2011; *Rempe et al.*, 2013; *Muto et al.*, 2015]. Similar types of pulverized rock were also observed on the Arima-Takatsuki Tectonic Line [*Mitchell et al.*, 2011; *Muto et al.*, 2015] and the Nojima fault [*Boullier*, 2011] in Japan and along the North Anatolian fault in Turkey [*Dor et al.*, 2009] (Figure 4.2). Pulverized rocks have been identified in other lithologies as well. Pulverized limestone has been observed in inactive normal faults in Israel [*Sagy and Korngreen*, 2012] and in the Venere normal fault [*Agosta and Aydin*, 2006] in Italy. Pulverized dolostone is present in the Foiana fault [*Fondriest et al.*, 2015] in Italy (Figure 4.2). Pulverized sandstones are observed along the San Andreas fault [*Dor et al.*, 2006b, 2009] and near a small fault related to the Upheaval Dome impact event [*Key and Schultz*, 2011] (Figure 4.2). This last observation is unique because this fault was formed during a single meteor impact event.

A microstructural and geometric analysis was performed on pulverized sandstones from the San Andreas fault [*Dor et al.*, 2009]. The fracture damage is not homogeneously distributed over the quartz grains but is concentrated in several grains while others stay relatively intact (Figure 4.3a, b). The fractured grains show a Hertzian-like fracture pattern, indicating a compressional setting. Therefore, a grain-by-grain analysis rather than a bulk PSD was obtained, thus excluding any comparison with PSDs from igneous crystalline rock. A trend of decreasing damage with increasing distance from the fault was observed. *Key and Schultz* [2011] obtained a PSD in pulverized sandstone with a *D*-value increasing from 0.77 for the original grain size to 1.55 for the pulverized rocks. This value is within the range measured for gouges [*Keulen et al.*, 2007; *Stünitz et al.*, 2010; *Muto et al.*, 2015] rather than for igneous pulverized rock ($D > 1.92$).

Pulverized limestones and dolostones have not yet been subjected to geometrical analysis. Qualitatively, the fragments might be slightly larger than those of classic pulverized rocks [*Fondriest et al.*, 2015]. Also, thin section images reveal a hierarchy of fractures, and rather than random fracture orientations they show a shard-and-needle structure (Figure 4.3c). In contrast, limestone samples from a borehole in Israel do not show any fracture hierarchy but dynamic fracture branching instead [*Sagy and Korngreen*, 2012] (Figure 4.3d). Fragment sizes of ~20 μm were observed in samples from this borehole, well within the fragment size range of crystalline rocks.

This raises the following question: Are these "pulverized" sandstone, limestone, and dolostone formations similar to the classic pulverized igneous rock or is it simply that these studies have used different and potentially confusing definitions? According to the field definition of *Dor et al.* [2006b], the other lithologies are not strictly pulverized (e.g., no powdery flour texture for limestones, no pervasive fracture damage but more localized fractures for sandstone). On the microscale, geometrical differences exist between the lithologies, although current knowledge on the quantitative geometrical constraints in

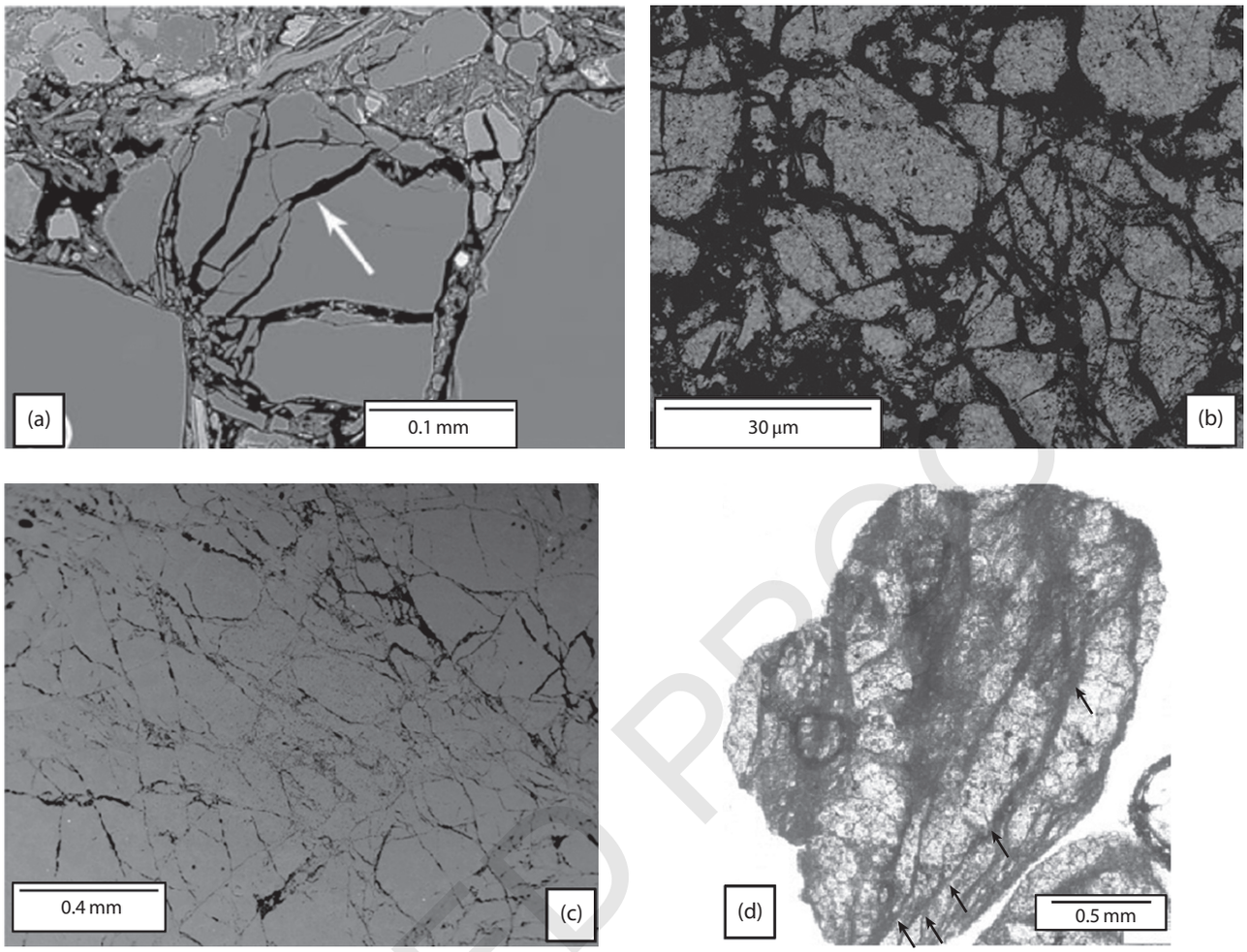

Figure 4.3 (a), (b) Microphotographs of pulverized sandstones. (a) Shows Hertzian fractures in a quartz grain at the contact with another grain. Note that surrounding grains do not show any fracture damage. (b) Pulverized quartz grains with varying degrees of damage. (c) Photomicrograph of pulverized dolostone, showing hierarchical fractures and some needle- or shard-type fragments. (d) Photomicrograph of a pulverized limestone from a borehole in Israel showing very small-size dynamic branching (black arrows) Sources: (a) *Dor et al.* [2009], (b) *Key and Schultz* [2011], (c) *Fondriest et al.* [2015], (d) *Sagy and Korngreen* [2012].

limestones and dolostones remains sketchy. Nonetheless, the fact that classic pulverized rocks show a seemingly isotropic and random damage fabric, while limestones and dolostones show a more angular, hierarchical, and anisotropic fabric and sandstones a localized and heterogeneous fabric, would seem to indicate a different mechanical response to similar loading conditions or to different loading conditions and thus a different origin of formation.

However, shared features such as the general lack of shear strain, the pervasive homogeneous or heterogeneous fracture damage distribution, and dilatational nature of the fractures point toward a common source related to nearby faults. All these considerations might be further clarified by completed or future experiments so as to monitor the whole formation process of pulverized rocks. Eventually, a clear definition for pulverized rock could then be proposed.

4.2.2. Pulverized Rock at the Fault System Scale

Pulverized rocks are mainly observed in mature fault systems with a large amount of total slip. Most of these fault systems are strike-slip, and the maximum distance from the fault plane where pulverized rocks have been observed is of the order of hundreds of meters (Figures 4.2 and 4.4). For mature fault systems (offset >10 km), the size of the pulverized zone is of the same order of magnitude as the width of the total damage zone [taken from *Faulkner et al.*, 2011; *Savage and Brodsky*, 2011] (Figure 4.4).

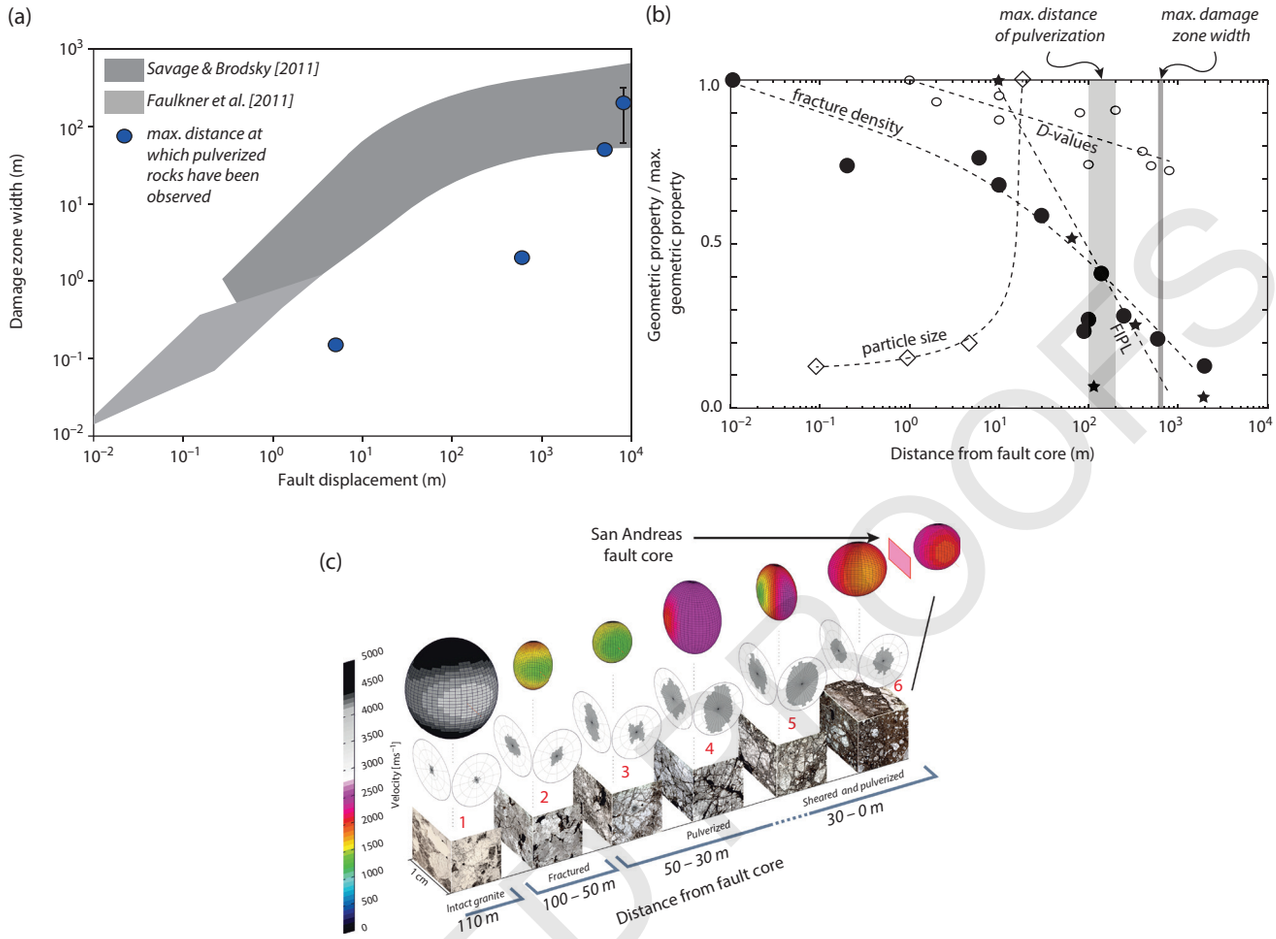

Figure 4.4 (a) Total displacement along the fault versus the width of the damage zone based on the compilation of data by *Savage and Brodsky* [2011] and extended by *Faulkner et al.* [2011]. Blue circles indicate approximate maximum distance of pulverized rocks from the fault core from several field studies (see Figure 4.2). All displacements greater than 10^4 m are clustered at 10^4 m, and these observations vary between 50 and 400 m, indicated by the error bar. (b) Several geometrical properties (normalized by the maximum value) versus distance from the fault core. The particle size is from pulverized San Andreas fault granite [*Rockwell et al.*, 2009], fracture density and D-values from the ATTL [*Mitchell et al.*, 2011; *Muto et al.*, 2015] and FIPL (Factor of Increase in Perimeter Length) measured on pulverized sandstone grains near the San Andreas fault [*Dor et al.*, 2009]. (c) Summary of anistropy within the damage zone of the San Andreas fault that includes pulverized rocks, obtained by *Rempe et al.* [2013]. Anisotropy is constrained by P-wave velocities (ellipsoids) and fracture orientations (rose diagrams). *See electronic version for color representation.*

The few observations of less-developed fault systems (offset <10 km) show that the maximum pulverization distance is several orders of magnitude less than the damage zone width. This might indicate that quasi-static or classic fault-related damage and dynamic damage or pulverization are not related to the same processes.

While the damage in damage zones may not be produced coseismically [*Mitchell and Faulkner*, 2009], pulverized rocks are thought to be created exclusively during earthquakes. Therefore, the magnitude of the seismic events, which, coupled with other factors, determines the dynamic loading conditions, can be taken into account instead of total displacement. For mature faults, earthquake magnitudes may be high (M_w >7). For faults with less overall offset, the maximum earthquake magnitude is usually less than $M_w = 7$. Here, the maximum pulverization distance from the fault is smaller as well. For the Upheaval Dome Impact structure [*Key and Schultz*, 2011], the magnitude is unknown but probably much greater than for tectonic faults of similar size. However, the number of observations of pulverized rock is still limited and the global dataset should be extended to confirm the trends of maximum pulverization distance from the fault in relation to total offset or earthquake magnitude.

Three studies have reported in situ observations of pulverized rocks at depth (Figure 4.2): ~40 m depth [*Wechsler et al.*, 2011], 5–6 km depth [*Sagy and Korngreen*, 2012], and 225–625 m depth [*A.-M. Boullier*, pers. comm]. For the last-mentioned author, constraints on laumontite-cement in the dilatant fractures show that the depth at the time of fracturing was between 3 and 8 km [*A.-M. Boullier,* pers. comm.]. Geological constraints on the depth of formation set from surface observations at the San Andreas fault indicate a maximum depth of about 4 km [*Dor et al.,* 2006b] and a minimum depth near the surface [*Dor et al.,* 2009]. Pulverized rocks are therefore a relative shallow crustal feature in the upper part of the seismogenic zone (<10 km depth).

Pulverized rocks are occasionally observed along bimaterial fault interfaces, where the pulverized rocks are distributed asymmetrically with a higher abundance on the stiffer side of the fault [*Dor et al.*, 2006a, 2006b, 2008; *Mitchell et al.*, 2011]. This does not exclude the presence of pulverized rock on the compliant side of the fault [*Dor et al.*, 2006b]. It is suggested that this asymmetric distribution of pulverized rocks is a strong argument in favor of a preferred rupture direction [*Dor et al.*, 2006a, 2008]. However, the response to dynamic loading of the lithology on the compliant side might be completely different to the response of the stiffer lithology, so that the presence of pulverized rocks might depend on lithology rather than on preferred rupture direction. Again, experimental work would help answer these issues. Other observations of pulverized rocks indicate no mechanical contrast across the fault, for instance, at the Nojima fault [*Boullier*, 2011 and pers. comm.].

Several studies have focused on the place of pulverized rocks within the damage zone and the transition from nonpulverized to pulverized rock. This is either achieved by geometrical constraints [*Dor et al.*, 2009; *Rockwell et al.*, 2009; *Muto et al.*, 2015], by measuring P-wave velocities [*Rempe et al.*, 2013], or by mapping fracture densities [*Mitchell et al.*, 2011; *Rempe et al.*, 2013]. In addition, permeability measurements have been performed [*Morton et al.*, 2012]. Regarding the fracture densities and geometric properties (Figure 4.4b), there is no clear or sudden transition from fractured rocks to pulverized rocks. Instead, within the sample resolution obtained, these properties evolve continuously from a background intensity outside the damage zone toward a peak intensity (high *D*-value or high fracture density) near the fault plane. Mean particle size measurement reveals a reverse trend: particles are larger the farther they are away from the fault. Close to the fault, pulverized rocks become more sheared and evolve toward cataclasite and gouge [*Rempe et al.*, 2013]. The fracture density decreases for these sheared cataclasites (Figure 4.4c).

Surprisingly, despite having the highest fracture density, pulverized rocks yield higher P-wave velocities than their less fractured peers located farther from the fault core [*Rempe et al.*, 2013] (Figure 4.4c). Also, changes in permeability are less straightforward than expected: a nonlinear increase of several orders of magnitude with increasing fracture density is observed on samples taken at the surface of the San Andreas fault zone. However, for the last few meters of intensely pulverized rocks, the permeability drops dramatically despite even higher fracture densities [*Morton et al.*, 2012]. These observations are strong arguments in favor of treating pulverized rocks differently from fractured damage zone rocks.

A last but important note should be made on the general description of "a large number of fractures that are oriented seemingly randomly": the fracture density count by *Rempe et al*. [2013] was performed on oriented samples so that fault-parallel and fault-perpendicular density could be established. This shows an anisotropic distribution of fractures with more fractures oriented fault-parallel than fault-perpendicular (Figure 4.4c). This is supported by the P-wave velocity measurements taken during the same study on similarly oriented samples: higher velocities are measured fault-parallel than fault-perpendicular, both in fractured and in pulverized samples. Thus, strictly speaking the classically pulverized rocks contain a nonisotropic damage distribution.

4.3. COSEISMIC OFF-FAULT DAMAGE BY ANALOGOUS LABORATORY EXPERIMENTS

The observations and analyses performed on the field samples described above only show the end product of coseismic loading in the case of pulverized rock and the end product of coseismic loading and fault sliding in the case of cataclastic rock. To constrain the mechanical conditions under which pulverized rocks can be created, laboratory tests are required. Such tests are based on the consideration that a sample loaded by an incoming stress wave, either in tension or compression, is analogous to the response of near-fault rocks to high-frequency waves during an earthquake.

To design such experiments, the approximate conditions and processes at which pulverized rocks are created first need to be considered. For this purpose, a short overview will first be given of the response of brittle material to a broad range of strain rates in order to illustrate the context of the problem at hand. The most suitable apparatus, the Split-Hopkinson Pressure Bar, for testing the origin of pulverized rocks will then be discussed.

4.3.1. General Overview of the Strain Rate Sensitivity of Geomaterials

Geological materials have been fractured over a wide range of strain rates, from 10^{-6} to $10^{6}\,s^{-1}$. From these experiments, a generalized conceptual failure model has been produced in which strain rate sensitivity has been

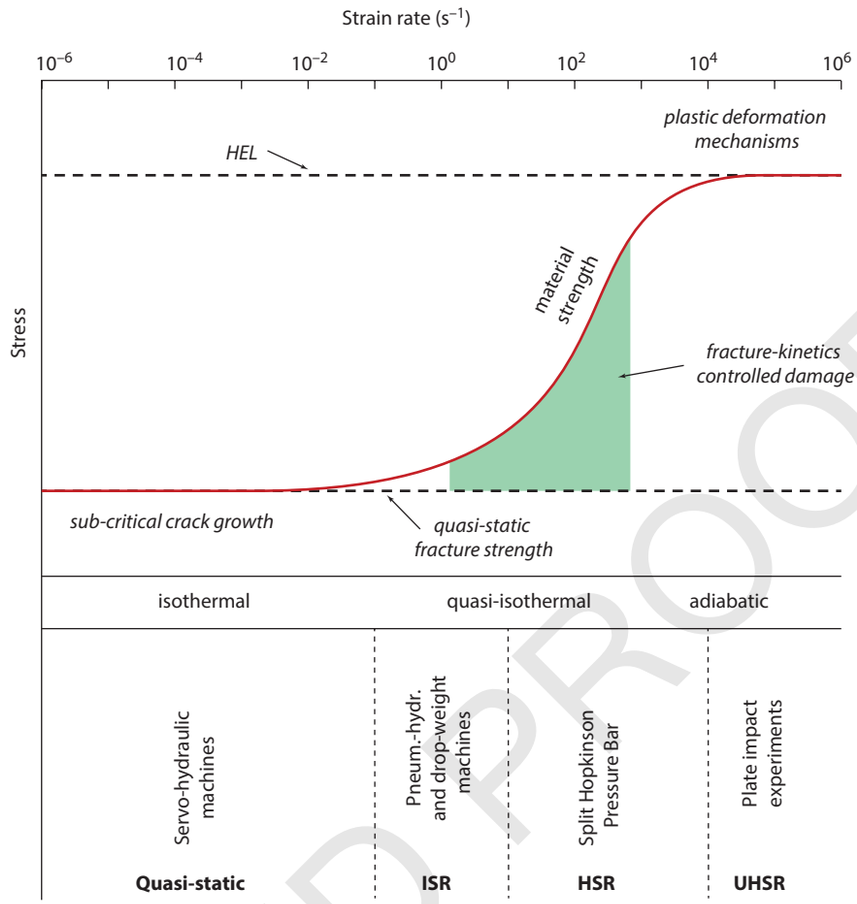

Figure 4.5 Failure strength of materials for a broad range of strain rates. The strain rate values are broadly applicable to geological materials at or near the surface. Two different failure horizons are crucial: the quasi-static strength and the Hugoniot Elastic Limit. Four failure regimes are indicated: subcritical crack growth, quasi-static failure, fracture-kinetics controlled failure and shock-related plastic failure mechanisms. A suitable experimental loading apparatus is indicated for the various strain rates. The appropriate terms for the strain rate testing fields are ISR = intermediate strain rate, HSR = high strain rate, UHSR = ultra high strain rate. Adapted from *Grady* [1998] and *Zhang and Zhao* [2013a].

incorporated [*Grady et al.*, 1977; *Grady*, 1998]. Two failure surfaces are essential for the failure of rock materials (Figure 4.5): the quasi-static fracture limit and the Hugoniot Elastic Limit (HEL).

At the lowest strain rates ($<10^{-6}$ s^{-1}), materials fail under isothermal conditions at relatively low stresses equal or less than the quasi-static fracture limit. Subcritical crack growth phenomena often play a major role in these conditions. At conventional laboratory strain rates ($10^{-6} - 10^{-1}$ s^{-1}), materials show little to no strain rate sensitivity and fail in a brittle manner at the quasi-static peak strength. The Griffith failure criterion (or models that have been developed from it) can predict the failure strength relatively accurately in terms of the activation and propagation of a critical flaw or a population of flaws (section 4.4.1).

At intermediate to high strain rates ($10^{-1} - 10^{4}\,s^{-1}$), the failure strength is strongly strain-rate dependent and the materials fail under quasi-isothermal conditions. This is due to inertia effects, which affect the fracture kinetics and allow transient loads or stress waves to exceed the quasi-static fracture limit (Figure 4.5). Due to this time-dependence of fracturing, several additional fractures have time to develop in addition to the weakest flaws, leading to a more diffuse fracture pattern. Models explaining fracturing within this fracture-kinetics controlled regime are discussed in section 4.4.

Once the inertial fracture delay has exceeded a certain threshold with respect to the loading rate (strain rates $> 10^{4} - 10^{5}\,s^{-1}$), the material can go beyond the second failure surface: the HEL (Figure 4.5). Above this elastic limit, a range of alternative failure mechanisms are

activated, such as crystal plasticity and formation of micro-shear zones filled with nano-particles [*Grady*, 1998]. Moreover, the adiabatic conditions can result in local melting, leading to a drastic drop in the rock friction coefficient [*Di Toro et al.*, 2004]. Effectively, the HEL represents a high strain rate version of the brittle-ductile transition. The HEL is insensitive to changes in strain rate [*Grady et al.*, 1977; *Grady*, 1998].

Since the pulverized rocks observed in the field lack plastic deformation and partial melting, loading conditions close to and beyond the HEL are unlikely to cause pulverization. The pervasive fracture textures suggest that the pulverized rock forms in the fracture-kinetics-controlled strain-rate-strength domain (Figure 4.5). Experiments in this strain rate range involve the intermediate strain rate (ISR, strain rate $10^{-1}-10^{1}\,s^{-1}$) and high strain rate (HSR, strain rate $10^{1}-10^{4}\,s^{-1}$) testing fields [*Zhang and Zhao*, 2013]. For ISR testing, pneumatic-hydraulic and drop-weight machines can be used; for HSR testing the most commonly used apparatus is the Split-Hopkinson Pressure Bar. This apparatus can be adjusted so that it includes the strain rate range of drop-weight machines, extending its range to lower strain rates of $10^{0}\,s^{-1}$. It has been used in all studies on pulverized rocks up to date.

4.3.2. Coseismic Damage by Compressional Loading Experiments

The Split-Hopkinson Pressure Bar (SHPB) apparatus (also known as Kolsky-bar) was developed in its current form by *Kolsky* [1949]. Given the relative novelty of this machine and its importance in all studies that have been performed up to date, the following section covers the basics of the apparatus. Specific attention is given to the manipulation of the imposed compressional stress wave. The current state of the art on dynamic loading experiments in relation to pulverized rocks is then summarized and discussed.

4.3.2.1. Methodology of the Split-Hopkinson Pressure Bar Apparatus

4.3.2.1.1. General Setup and Mechanical History by 1D-Wave Analysis A typical SHPB setup includes an input bar and an output bar supported by low-friction ball bearings or Teflon-coated uprights (Figure 4.6a, b). The rock sample is placed between the two bars and can be held in place by a lubricant. A launch mechanism (gas gun, spring gun) accelerates a striker toward the input face of the input bar. The velocity of the striker depends on the launch mechanism: a spring gun produces lower velocities and is used to perform reproducible tests at lower strain rates ($10^{0}-10^{3}\,s^{-1}$) than a gas gun ($10^{2}-10^{4}\,s^{-1}$). At impact, a compressive planar stress wave is created that travels through the input bar (Figure 4.6a). Typically the wave has a duration of less than 1 millisecond. This incident wave splits into a reflected wave and a transmitted wave at the input bar-sample interface (Figure 4.6a). The reflected wave travels back through the input bar, the transmitted wave travels through the sample and into the output bar (Figure 4.6a). Both transmitted and reflected waves then travel end-to-end in their respective bars.

In order to obtain the full stress-strain loading history, the propagation of the planar stress waves is recorded first. For this purpose, strain gauges are placed on the input and output bars (Figure 4.6a). The acquisition frequency of the gauges must be sufficiently high to ensure that the stress wave loading is monitored in acceptable detail (e.g., a frequency of 1–2 MHz). The strain gauges are placed on the bars at specific distances from their extremities so that the incident, reflected, and transmitted waves are recorded without overlap.

The raw data record is then preprocessed by identifying the first passage of the three waves (incident, reflected, and transmitted, Figure 4.6c). The first two waves are recorded on the input bar, where by definition the first signal is the incident wave and the remaining signals are the back-and-forth traveling reflected wave. The output bar contains exclusively the transmitted wave signal. Only the primary recordings of the reflected and transmitted waves are needed. The equation describing stress wave propagation along a thin bar is known as the Pochhammer-Chree equation [*Graff*, 1991], so that the three waves can be numerically projected backward (transmitted and reflected wave) and forward (incident wave) to the edges of the bars, and hence to the edges of the sample (Figure 4.6d).

The loading history is obtained by applying a 1D-wave analysis [*Graff*, 1991; *Chen and Song*, 2011]. The stress history is obtained by resolving the forces acting on the bar-sample interfaces for each wave (Figure 4.6e) (subscript I, R and T for incident, reflected and transmitted wave respectively). All symbols used in the formulas in this review are listed in Table 4.1. The force F is given by

$$F_{I/R/T} = -E_B A_B \times \varepsilon_{I/R/T}, \tag{4.1}$$

where E_B is the Young modulus of the bar material, A_B is the surface area of the bar extremities, and ε is the strain gauge data of the stress wave (the minus sign comes from the convention that the dilatational strain recorded by a strain gauge is positive). The stress (σ) acting on the surfaces of the sample is computed as a simple force balance divided by the surface area of the sample (A_S). For the sample output surface this is

$$\sigma_{out} = -\frac{F_T}{A_S} = -\frac{E_B A_B}{A_S}\left(\varepsilon_T\right). \tag{4.2}$$

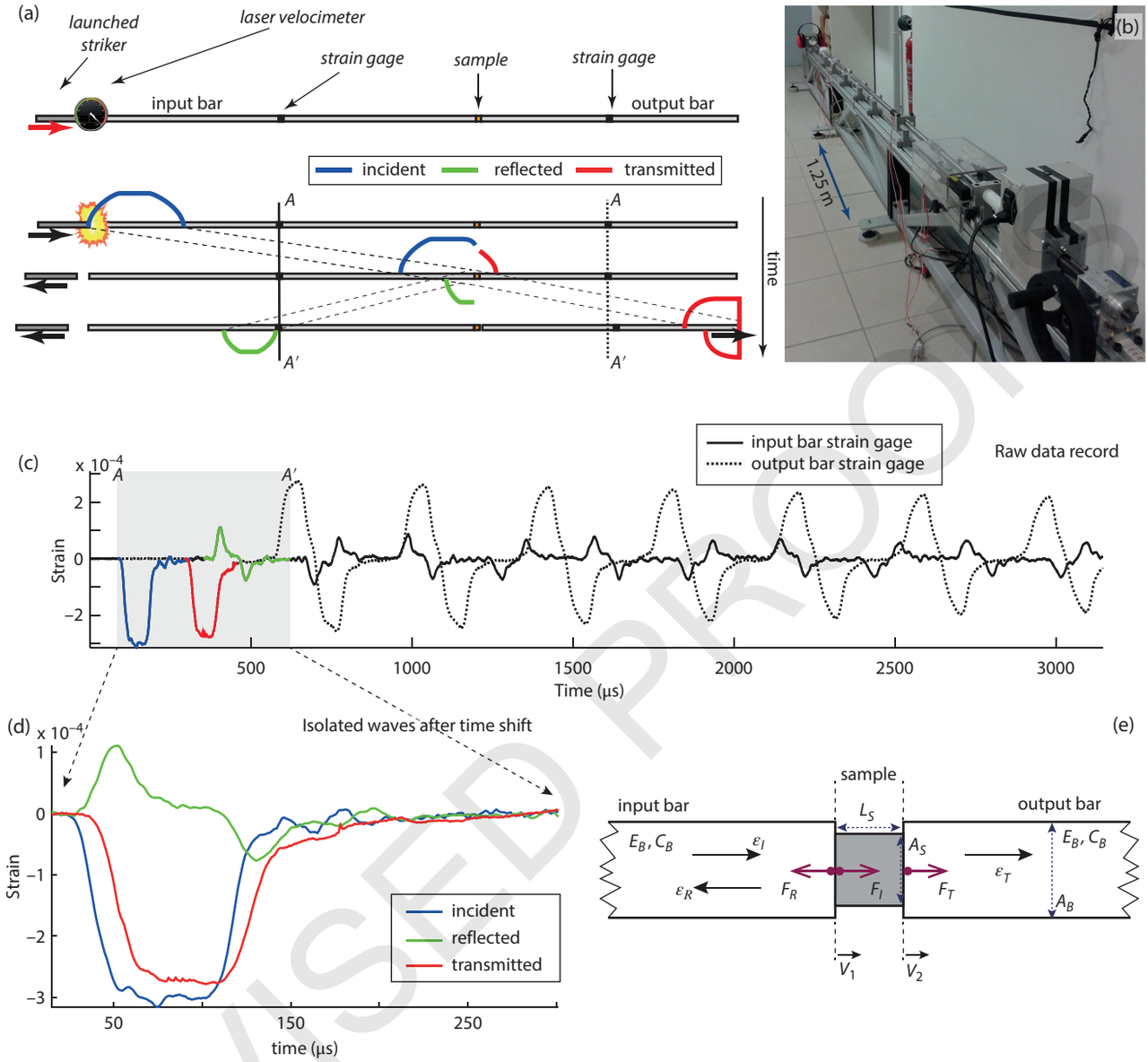

Figure 4.6 (a) Sketch of a typical Split-Hopkinson Pressure Bar (SHPB), in this case a mini-SHPB with a spring gun as launching system. The velocimeter records the speed of the striker bar and triggers the data acquisition system. Strain gauges record the incident (blue), reflected (green), and transmitted (red) stress waves as they travel along the length of the bars, as indicated by the three time snapshots. A–A′ indicates the time interval highlighted in gray in figure (c). (b) Photograph of a mini-SHPB apparatus at the ISTerre laboratory in Grenoble. (c) Raw data record of the input bar (black) and output bar (black dashed). The gray area corresponds to A–A′ in figure (a) and encompasses the primary passing of the three stress waves, which are highlighted in color. The record shows no second loading because the transmitted and reflected waves do not show a sharp alteration in shape and intensity. (d) The incident, transmitted, and reflected waves after the time shift from the gauge locations to the bar interface. (e) Sketch of the sample and sample-bar interfaces with the bar properties and the direction of strain pulses, particle velocities, and forces. See text and equations (4.1)–(4.6). Figures (c) and (d) show a test during which a quartz-monzonite sample was deformed in the elastic regime. *See electronic version for color representation*.

And for the input surface:

$$\sigma_{in} = -\frac{F_I + F_R}{A_S} = -\frac{E_B A_B}{A_S}\left(\varepsilon_I + \varepsilon_R\right). \quad (4.3)$$

Note that the reflected wave has an opposite (tensional) strain and is thus effectively subtracted from the incident wave. Equations (4.2) and (4.3) are called the 1-wave analysis and 2-wave analysis, respectively. If the assumption of stress equilibrium along the length of the sample is satisfied, a 3-wave analysis yields the mean stress on the sample:

$$\sigma_{mean} = -\frac{F_I + F_R + F_T}{2A_S} = -\frac{E_B A_B}{2A_S}\left(\varepsilon_I + \varepsilon_R + \varepsilon_T\right). \quad (4.4)$$

However, in practice initial stress equilibrium issues render the 2-wave and 3-wave analyses less reliable. Use of the 1-wave analysis is recommended for testing brittle samples.

Strain and strain rate are computed from the relative difference in particle velocities of the input bar-sample interface (v_1) and the output bar-sample interface (v_2) (Figure 4.6e). These velocities are given by

$$\upsilon_1 = c_d^B\left(-\varepsilon_I + \varepsilon_R\right) \quad \upsilon_2 = -c_d^B\varepsilon_T, \quad (4.5)$$

where c_d^B is the P-wave velocity of the bar material. The relative difference in velocity divided by the sample length (L_S) then gives the strain rate

$$\dot{\varepsilon} = \frac{\upsilon_1 - \upsilon_2}{L_S} = \frac{c_d^B}{L_S}\left(-\varepsilon_I + \varepsilon_R + \varepsilon_T\right). \quad (4.6)$$

A time integration of equation (4.6) gives the strain. For more details on 1D-stress analysis, see *Graff* [1991], *Gama et al.* [2004], and *Chen and Song* [2011].

4.3.2.1.2. Assumptions and Pitfalls of 1D-Wave Analysis To ensure a valid 1D-wave analysis for brittle samples, the following assumptions must be verified [*Zhao and Gary*, 1996; *Gama et al.*, 2004; *Chen and Song*, 2011; *Zhang and Zhao*, 2013]:

1. The stress wave propagation in the bar is 1D and longitudinal to the bar axis.
2. Stress is in equilibrium along the length of the sample during deformation.
3. Friction and radial inertia effects are kept minimal.
4. The sample is loaded once per test.

1D longitudinal wave propagation: Since the deformation history is obtained by 1D-wave analysis, this assumption is imperative. However, in an experimental setup there are always small alignment issues so that the bar interfaces are not perfectly perpendicular to the stress wave propagation direction. Carefully aligning and calibrating the apparatus before an experiment reduces this error. Keeping the length/diameter ratio of the bars greater than 20 and input wave stresses below the elastic limit of the bar can further ensure 1D wave propagation.

The finite diameter of the bars causes dispersion of the stress waves in the bar by the appearance of multiple propagation modes [*Graff*, 1991]. This will affect especially the higher frequency components in the stress wave, which will travel more slowly than the lower frequency components. Thus, the stress wave measured at the strain gauge is different from the actual stress wave at the bar-sample interfaces. This dispersion can be described by the Pochhammer-Chree equations [*Graff*, 1991], and since in practice only the first propagation mode is activated, the stress wave dispersion can be modeled relatively easily. From this, the stress wave is corrected for the position at the sample-bar interfaces.

Stress equilibrium along the length of the sample: This assumption must be valid for the three-wave stress analysis to be applied. Also, a sample in stress disequilibrium might result in heterogeneous deformation: for instance, the input side of the sample might be fractured while the stress at the output side of the sample never exceeds the elastic limit. Given that at the onset of loading, a sample is always in stress disequilibrium for the duration of a "ring-up" period or equilibrium time [*Nemat-Nasser et al.*, 1991; *Zhang and Zhao*, 2013], it is crucial to know the stress level when equilibrium has been reached. Typical equilibrium times are at least four times the transit time [*Ravichandran and Subhash*, 1994] or π times the transit time [*Davies and Hunter*, 1963]. The transit time is the one-way P-wave travel time through the sample.

A simple model can be used to check whether a loading has been in stress equilibrium before nonelastic deformation has set in, based on linear elastic behavior and wave reflections [e.g., *Ravichandran and Subhash*, 1994]. In such models, the expected elastic behavior is then compared to the actual loading history, and the necessary adjustments can be made for further testing. The input data for such models are the bar material properties, sample length, and an estimate of the density and P-wave velocity of the tested material. Analysis of these models shows that the sample length, impedance mismatch between bar and specimen, and most importantly, the shape of the incident pulse in the early stages of loading, influence the equilibrium time. The manipulation of the incident pulse is discussed in detail in the next section.

Friction and radial inertia effects: A lubricant at the bar-sample interface can reduce friction at this interface. During dynamic loading, radial inertia gives rise to extra axial stress components and therefore results in radial confinement. This effect can be minimized by keeping the length/diameter ratio of the sample equal to or less than

one [*Gama et al.*, 2004; *Chen and Song*, 2011; *Zhang and Zhao*, 2013]. With increasing sample diameter, the radial and axial stress components increase [*Forrestal et al.*, 2007; *Chen and Song*, 2011]; thus, samples with a small diameter experience less inertia-related additional stress components.

Single loading per test: A second loading during a single test may be preferred in some cases but increases the difficulty in performing the 1D-wave analysis preprocessing due to wave overlapping. The occurrence of a second loading can be checked from the raw data record: the transmitted and reflected waves would record a sudden change in shape and amplitude in such a case. The risk of this happening can be reduced by installing a momentum trap [*Zhang and Zhao*, 2013] or reducing the length of the output bar so that it moves away from the sample before reloading from the input bar.

4.3.2.1.3. Manipulation of the Incident Stress Wave Loading conditions of a high strain rate test are defined by the stress magnitude, the loading duration, and the loading rate of the incident wave. A "standard" incident wave created by the impact of two similar bars is trapezium shaped. Here, we discuss how to manipulate this trapezium-shaped wave so that a reliable high strain rate test can be designed.

The magnitude of the incident wave determines the stress on the sample. The most straightforward way to adapt this is by changing the speed of the striker at impact (Figure 4.7a). A good approximation of the stress magnitude in an incident wave is given by the following equation for the impact of two similar bars [*Graff*, 1991]:

$$\sigma = \frac{\rho_B c_d^B}{2} \upsilon_B, \tag{4.7}$$

where v_B is the speed of the bar at impact and ρ_B is the density of the bar material. This shows that, besides the speed at impact, the striker and/or bar material also influences the magnitude of the incident wave (Figure 4.7c).

The duration of the incident wave depends on the P-wave velocity of the material and on the pulse length. The pulse length is given by twice the length of the striker [*Graff*, 1991]. Thus, by changing bar material or by increasing the striker length, the loading duration can be modified and controlled (Figure 4.7c). However, the finite length of the bars needs to be taken into account: when the loading duration is nearly equal to the distance between strain gauge and sample, the incident and reflected waves might overlap, making it impossible to clearly identify and isolate the different waves. Moreover, a longer loading duration might cause a switch from dynamic loading to quasi-static loading once the stress pulse has reached a plateau of constant stress. It depends on the aim of the research if this is expedient.

It is crucial to control the loading rate on the sample to ensure that stress equilibrium is reached before nonelastic deformation occurs (see section 4.3.2.1.2). In addition, the dynamic mechanical properties of rocks are highly sensitive to loading rate or strain rate. As described above, the wave velocity (solely dependent on the P-wave velocity of the bar material) determines the loading duration. This means that a slower wave imposes a slower loading rate compared to a faster wave with equal magnitude and equal length. A change in magnitude also influences the loading rate. However, both variables significantly change the other loading conditions as well (loading duration and stress magnitude), which might be undesirable.

Therefore, the most powerful tool to manipulate the shape of the incident wave is the use of pulse shapers (Figure 4.7b). Pulse shapers are thin discs of a softer material. The impedance mismatch between the striker and the pulse shaper results in smoothing of the incident wave. Also, the thickness of the pulse shaper has to be taken into account: the thicker the pulse shaper, the more muffled the incident wave will become. The pulse shaper technique is highly suited to solving stress disequilibrium problems since it decreases the loading rate at the beginning of loading.

4.3.2.2. Rock Pulverization in Compression by Split-Hopkinson Pressure Bar experiments

Several studies on the dynamic compressional behavior of geological materials have been performed using the SHPB apparatus (Figure 4.8a, adapted from *Zhang and Zhao*, 2013). Many of these studies are from the (geo-) engineering or material science community and are not necessarily focused on coseismic damage and implications on fault behavior. Studies that do are scarce and are performed on crystalline granitic rock [*Doan and Gary*, 2009; *Yuan et al.*, 2011; *Doan and D'Hour*, 2012] or on Carrara marble [*Doan and Billi*, 2011] (Figure 4.8).

All crystalline geological materials show a single trend (Figure 4.8a): the dynamic peak strength of the sample increases with increasing strain rate. This confirms that the loadings are performed within the kinetics-controlled fracturing regime (Figure 4.5). The increase in strength of limestone and marble is stronger compared to granitic and basaltic rock at similar strain rate. However, it should be noted that the true uniaxial compressive strength is not known for each study; in this case, the data is normalized to the lowest dynamic strength value from that particular study.

Besides the increase in strength of rock material with higher strain rates, the (macroscopic) end-state also

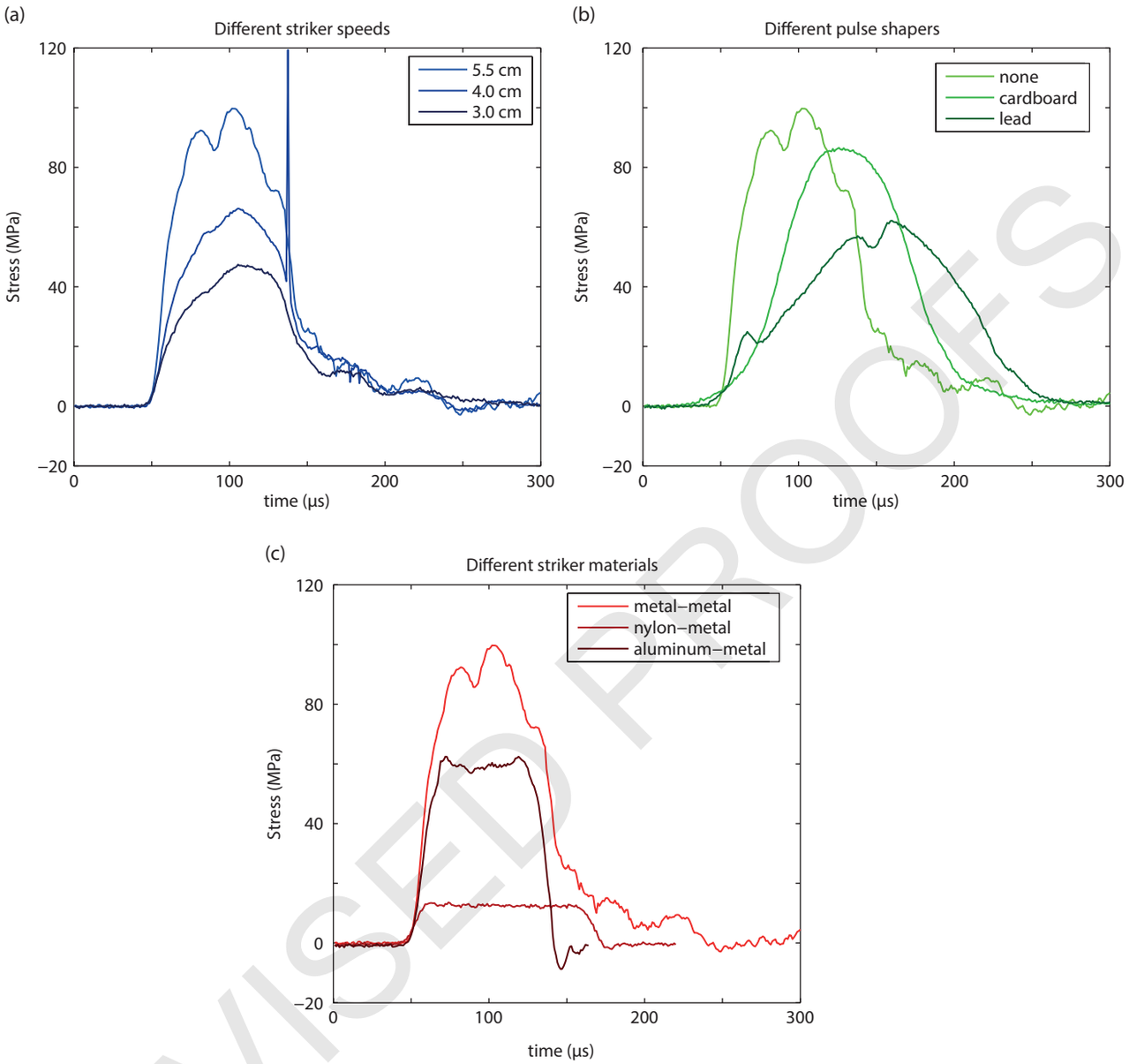

Figure 4.7 Raw incident stress waves (no dispersion correction) produced by (a) steel-steel impact from a 20 cm striker with varying speeds (expressed as spring gun loading distance). (b) Stress waves produced by steel-steel impacts from a 20 cm striker, with addition of cardboard or lead pulse shapers. (c) Stress waves produced by the impact of a striker made from various materials (steel, aluminium, nylon) onto a steel bar.

changes. Failure end-states can be classified as intact, split (single or few fractures), and pervasively fractured/pulverized [*Li et al.*, 2005; *Xia et al.*, 2008; *Doan and Gary*, 2009]. *Doan and Gary* [2009] reported that the transition from split to pulverized is defined by a pulverization strain rate threshold between 100 and 150 s^{-1} (Figure 4.8b). This was determined on San Andreas granites (the protoliths of the pulverized rocks observed by *Dor et al.*, [2006b]), which showed a large amount of initial fracture damage. Less damaged Tarn granites proved to have a pulverization strain rate threshold that was nearly twice as high (~250 s^{-1}) [*Doan and D'Hour*, 2012] (Figure 4.8b). A similar strain rate was obtained on Westerly granite in unconfined condition [*Yuan et al.*, 2011]. Pulverization has been shown to occur at a higher strain rate when the samples experience confining

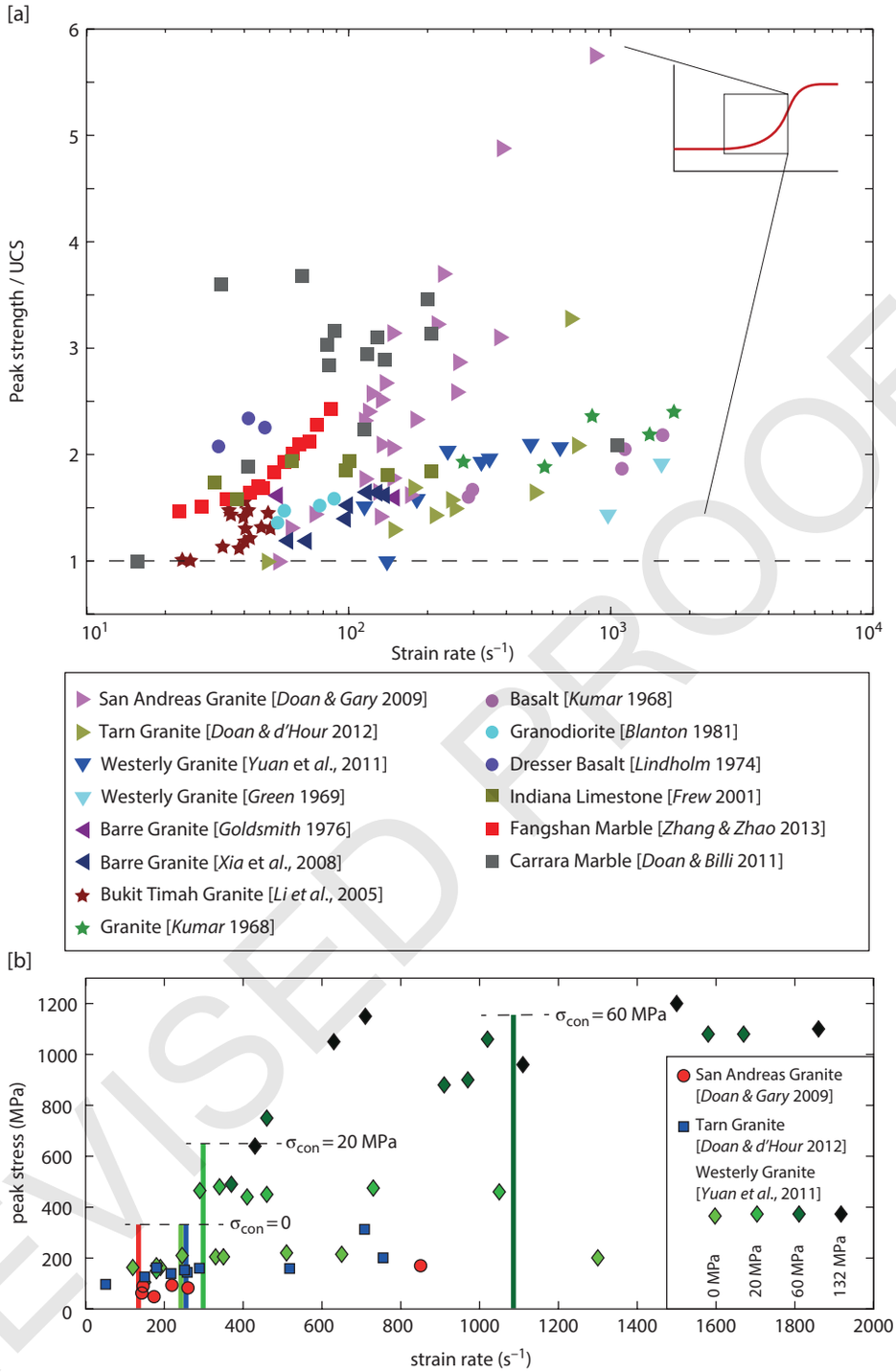

Figure 4.8 (a) Compilation of dynamic compressive loading data obtained by SHPB experiments on geological materials [*Green and Perkins*, 1968; *Kumar*, 1968; *Lindholm et al.*, 1974; *Goldsmith et al.*, 1976; *Blanton*, 1981; *Frew et al.*, 2001; *Li et al.*, 2005; *Xia et al.*, 2008; *Doan and Gary*, 2009; *Doan and Billi*, 2011; *Yuan et al.*, 2011; *Doan and D'Hour*, 2012; *Zhang and Zhao*, 2013b]. The data fall within the kinetics-controlled fracturing regime (small inset top right). Figure modified from *Zhang and Zhao* [2013]. Note that the true UCS was not known for all data series; in this case, the strength has been normalized to the lowest dynamic strength. (b) Strain rate versus peak stress plot showing data of studies that specifically focus on pulverization in igneous crystalline rock. The colored vertical bars indicate the pulverization strain rate thresholds. The confining stress is indicated for the experiments by *Yuan et al.* [2011]. Note that the unconfined pulverization thresholds from the different studies cluster around 200 s^{-1}, except for the initially damaged San Andreas granite samples.

pressure during loading [*Yuan et al.*, 2011] (Figure 4.8b). On the other hand, the pulverization strain rate threshold can be lowered by performing successive dynamic loadings with strain rates below the initial pulverization strain rate threshold, establishing a new pulverization threshold that is 50% lower, from 180 s^{-1} to 90 s^{-1} [*Aben et al.*, 2016].

However, three points regarding the pulverization of rocks in the studies mentioned above require some discussion. First, a qualitative method rather than quantitative measurements has been used to determine whether the sample is split or pulverized, although in practice the transition from a split sample (e.g., less than 10 fragments) to a pulverized sample is very clear, and difficulties in labeling them are rare.

Second, *Yuan et al*. [2011] imposed a confining pressure on the samples by using tight-fitting sleeves of different materials (Poly[methyl methacrylate], copper, brass). The authors assumed that the confining sleeves behaved as a perfect elastic material, and from this they derived the confining stress theoretically. Confining stresses as high as 132 MPa were reached. However, they did not measure the actual mechanical behavior of the sleeve (unlike *Forquin et al*. [2010]). Therefore, the true confining pressure during deformation is difficult to define and might deviate from their reported values. Nonetheless, the trend of an increasing pulverization strain rate threshold with increasing confining pressure is clear (Figure 4.8b).

Third, the strain rate histories during dynamic loading experiments are complex (Figure 4.9), since SHPB experiments are too fast to be servo-controlled. Moreover, when a sample is qualitatively pulverized, the strain rate history includes an extra strain rate peak after the initial strain rate peak [*Xia et al.*, 2008; *Aben et al.*, 2016] (Figure 4.9). Various authors have picked different representative strain rates from this history. For instance, strain rates have been obtained by taking the maximum strain rate, excluding the second strain rate peak [*Doan and Gary*, 2009; *Doan and D'Hour*, 2012], by averaging the strain rate [*Yuan et al.*, 2011] or by taking the strain rate value of the constant strain rate plateau [*Xia et al.*, 2008]. No supporting evidence has been given to show that these strain rates are representative of dynamic fracturing. Linear elastic fracture mechanics, adjusted to dynamic loading conditions [*Bhat et al.*, 2012], were applied to experimental data by *Aben et al*. [2016] to show that the strain rate plateau in between the two strain rate peaks coincides with the onset of dynamic fracturing. This is supported by high-speed camera data that were synchronized with the acquisition system of an SHPB apparatus (Figure 4.9), which shows that the formation of fractures concurs with the strain rate plateau or hinge point. Thus, although the different strain rate thresholds (Figure 4.8b) seem to be consistent and within the same range, precision can be increased in future studies by picking similar representative strain rates according to a single convention.

A remarkable observation that distinguishes the experimentally pulverized rocks from the fragmented rocks is the strong reduction in the duration of the stress wave in the output bar (Figure 4.9a): from an initial duration of ~180 μs to ~90 μs in this example. Basically, the stress wave is "cut off" because the pulverized sample cannot transfer the stress anymore at atmospheric confinement. At higher confining pressures it is expected that the stress wave after pulverization will show a significant drop to a much lower stress amplitude. Such a reduction in the stress wave is not observed in the case of fragmented samples.

Microstructural analysis of postmortem crystalline samples shows very similar damage textures to field samples, with very little accommodated strain and pervasive fragmentation below grain size [*Yuan et al.*, 2011]. Grain size analyses performed on pulverized and fractured San Andreas and Tarn granite show that the mean particle size is greater than the values obtained on field samples [*Doan and Gary*, 2009]. This difference may be explained by the fact that the field samples have experienced several coseismic loadings and different stress states in between coseismic loadings.

The only other material tested for coseismic damage is Carrara marble [*Doan and Billi*, 2011]. Here again a transition from a fractured to a pulverized end-state has been observed qualitatively. The transition is not clearly indicative of a strain rate threshold: pulverization occurs from 68 s^{-1}, but this strain rate overlaps with apparently intact and split samples. The threshold is in fact expressed much more clearly in terms of strain: above 1.3% residual strain, the samples are pulverized. Carrara marble therefore pulverizes at milder loading conditions than crystalline mineral aggregates. The microstructures obtained after the experiments on Carrara marble show some plastic deformation by twinning before fracturing. No detailed geometric quantification has been performed.

The transition from split to pulverized rocks is also visible in the amount of energy that is dissipated with an increase in axial strain [*Doan and Billi*, 2011; *Aben et al.*, 2016]. The apparently intact and fractured samples plot along a line with a relatively steep slope (103 MJ/m^3 for Carrara marble). This slope decreases by more than 50% at higher strains, when samples have been classified as pulverized. This transition may reflect a change in dominant deformation mechanism. Hence, it may indicate the phase change from a crystalline material to a granular material: near the pulverization threshold the sample loses all cohesion and granular flow becomes the dominating mechanism for strain accommodation [e.g., *Lyakhovsky and Ben-Zion*, 2014]. When this process is inhibited immediately after this transition, the rock becomes cohesionless while the amount of accumulated shear strain is kept so that the original texture is preserved.

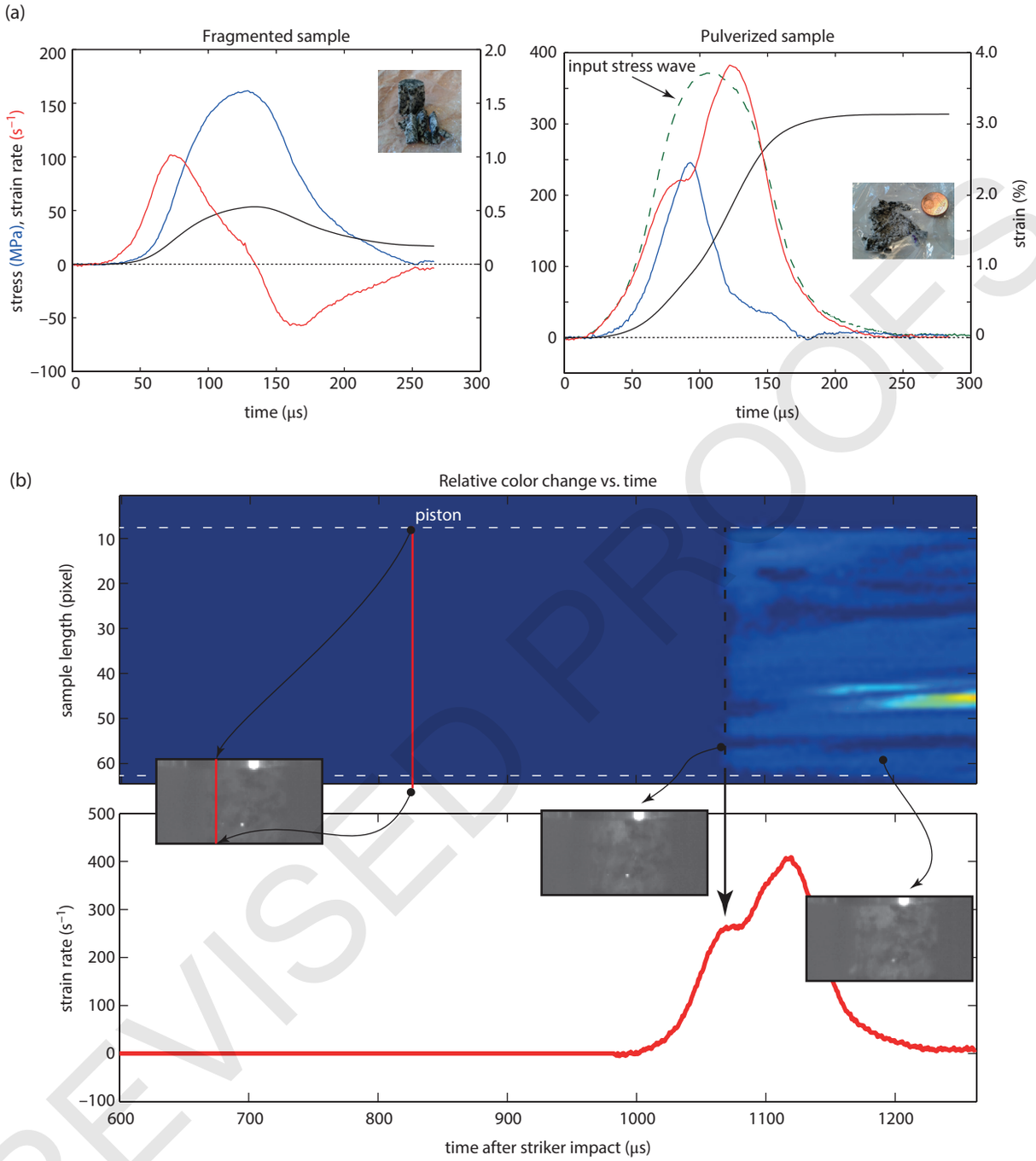

Figure 4.9 (a) Mechanical data of a fragmented (left) and a pulverized (right) quartz-monzonite sample [from *Aben et al.*, 2016]. The stress (blue), strain (black) and strain rate (red) parameters are plotted versus time. Note the distinctive difference in mechanical history, mostly expressed in the strain rate history, which includes a second strain rate peak in case of pulverization. The inset shows postmortem photographs of the samples. The input stress wave of the pulverized sample (green curve, vertically not to scale) highlights the reduction in period of the output stress wave (blue curve). (b) High-speed camera data (top) synchronized with the strain rate history (bottom) of a pulverized quartz-monzonite sample. The camera had an acquisition rate of 0.3 MHz, the mechanical data 1 MHz. Three camera stills from before, during, and after loading have been included. The top plot shows the relative color change along one column of pixels (indicated by the red line in the first still) with time. From this, it follows that fracturing initiates at the strain rate plateau (black arrow) between the initial peak and second strain rate peak. *See electronic version for color representation*.

Postloading petrophysical and geophysical properties were measured by *Aben et al*. [2016] on apparently intact and fragmented end-states. P-wave velocity measurements indicate a decrease in velocity in the axial direction as a function of dissipated energy. An even greater decrease is obtained for the radial directions, reflecting the development of an anisotropic damage structure in these samples. This is in accordance with measurements on field samples [*Rempe et al.*, 2013] (Figure 4.4c). The porosity measured on the same samples increases nonlinearly with increasing damage, suggesting some kind of percolation behavior for crack connectivity. Permeability measurements taken on dynamically fractured and pulverized samples show an initial increase in permeability with increasing amount of damage, followed by a sudden drop in permeability for jacketed pulverized samples [*Morton et al.*, 2012]. This observation matches permeability measurements on field samples. These two studies include not only pulverized samples but also dynamically fractured or split samples and suggest that a single high-magnitude earthquake [*Morton et al.*, 2012] or several successive earthquakes [*Aben et al.*, 2016] could create a damage zone structure as observed in the field. Section 4.5 discusses how the experiments are linked to fault mechanics and damage zone geometry.

4.3.3. Dynamic Tensile Loading SHPB Experiments

To date, no publications on dynamic tensile loading and pulverization are available. However, dynamic tensile loading experiments have been performed on brittle (geo-)materials in the civil engineering community [*Zhang and Zhao*, 2013 and reference therein]. Within the strain rate range of interest, most experiments are performed on modified versions of the classical SHPB apparatus. Either direct or indirect tensile tests can be performed, following different adjustments of the SHPB [*Zhang and Zhao*, 2013; *Xia and Yao*, 2015]. In general, tensile testing produces less reliable results than compressive loading.

Direct tensile tests typically involve an anvil or a similar construction attached to the input bar so that a striker can be launched onto it from the opposite direction compared to standard compressive SHPB tests. The sample is fixed between the input and output bars, either by epoxy glue or a screw system. Often, the sample-bar connection involves a complex sample shape (e.g., dumbbell or bone-shaped). The attachment and sample shape can cause several additional complexities regarding the assumption of stress equilibrium and the 1D-wave analysis apart from standard considerations (section 4.3.2.1.2). Moreover, manipulation of the input wave by pulse shaping techniques becomes harder.

Several indirect tension tests have been designed for the SHPB: the Brazilian disc method, the three-point bending technique, and spalling experiments [*Zhang and Zhao*, 2013; *Xia and Yao*, 2015]. The Brazilian disc method uses a disc of material wedged between the bars with the cylindrical surface in contact with the bar interfaces. The sample is consequently split between the contact points by a compressive stress wave loading. In the three-point bending technique, instead of a disc, a prism-shaped or semicircular sample is fixed so that the flat surface rests on two nipples attached to the output bar. For these methods, the loading and pulse shaping is similar to that of compressive tests. However, the three-point bending technique gives a flexural strength value rather than purely tensile strength. Also, stress equilibrium is hard to reach and verify due to the free surface area. The Brazilian disc and three-point bending methods are typically used for studying the initiation and propagation of single fractures. These single fracture methods are not very suitable since the concept of pulverized rocks requires the complexity and interaction of a large amount of fractures distributed in a volume.

The spalling test requires only a single bar on which a long slender sample is attached. A compressive stress wave travels through the bar and sample and then reflects at the free end of the sample. It then becomes a tensile stress wave that places the end of the sample under tension. For a reliable test, the amplitude of the stress wave must be lower than the compressive strength but higher than the tensional strength of the rock. This requirement, coupled with the need to monitor the stress wave dispersion in the long and often heterogeneous sample, is challenging.

Consequently, direct tensile dynamic experiments are the most interesting for generating pulverized rock. Results from such tests on geomaterials reveal that the tensional failure strength increases with strain rate [*Asprone et al.*, 2009; *Cadoni*, 2010; *Zhang and Zhou*, 2013]. The strength–strain rate curve starts rising between 10^0 and $10^1\,s^{-1}$, roughly one order of magnitude less than the compressional failure strength curve (Figure 4.8). Moreover, data from indirect tensile experiments show the curvature in the strength–strain rate data already between 10^{-1} and $10^0\,s^{-1}$ [*Zhang and Zhao*, 2013 and reference therein].

Postmortem samples from direct tensile dynamic tests typically show macroscopic failure along a single (mode I) fracture [*Asprone et al.*, 2009; *Cadoni*, 2010]. To our knowledge, there are no microscopic and microstructural analyses on postmortem samples available in the literature. Nonetheless, there are no reports of fragmented or pulverized end-states such as those observed on compressional dynamic loadings. It should be noted that direct tensile tests have been performed up to strain rates of $\sim 100\,s^{-1}$, which is below most pulverization thresholds that have been established for dynamic compressive loading.

Therefore, the question of whether the fracture-kinetics controlled regime for tensile loading results in less diffuse damage than the compressive fracture-kinetics regime, or whether pervasive tensile fracturing occurs at unexplored higher strain rates remains open to discussion and needs answering in the future.

Another possible experiment to generate pulverized rock, besides (uniaxial) compressive and tensile transient loading experiments, is hydro-fracturing due to a sudden drop in confining pressure. This would require the presence of a pressurized pore fluid pressure in the rock. During a transient drop in confining pressure, the difference between the pore fluid pressure and confining pressure can become equal or higher than the tensile strength of the rock so that the rock explodes due to the volumetric increase of the fluid. Note that the drop in confining pressure does not always result in a tensile state of confining pressure. Experiments that try to mimic this process involve rapid degassing of a gas-chamber with gas-saturated samples and are currently in a preliminary phase [*Mitchell et al.*, 2013].

4.4. DYNAMIC BRITTLE DAMAGE MODELS

4.4.1. Dynamic Versus Quasi-Static Damage: Strain Rate Effects on a Network of Microfractures

As discussed in section 3.1, coseismic damage is thought to be controlled by the kinetics of fracture network development. The high strain rate induced by the seismic waves will affect the collective behavior of the preexisting fractures present in the fault zone. Before discussing dynamic fracture damage, the processes controlling quasi-static fracturing will be reviewed and classical approaches for their modeling described.

For both static and dynamic loading, failure occurs through the following processes [*Paterson and Wong*, 2005, chap. 6]: (1) Nucleation of microfractures, which become activated, after which (2) the growth of microfractures is initiated. Initially, the fractures develop independently before they interact. (3) The interactions lead to stress shadowing and to the coalescence of microfractures to form a macroscopic fracture. Depending on the loading mode and the loading rate, each process has a different significance.

A tensile loading mode tends to initiate unstable mode I fractures that can propagate in the same direction without further increase in applied stress. The weakest flaw (e.g., pores, microcracks) in a sample will propagate and extend across the whole sample as soon as its stress intensity factor K exceeds a critical threshold value K_C, causing failure. This weakest flaw hypothesis, coupled with a power law distribution in flaw strength, gives the popular Weibull statistics of strength of a material [*Weibull*, 1939; *Wong et al.*, 2006].

A compressional loading mode leads to a different failure pattern where mode II cracks tend to deviate from their initial direction to become parallel to the principal stress direction. Any crack tilted relative to this direction will deviate from mode II to form a mode I wing crack whose progression is stable [*Nemat-Nasser and Horii*, 1982; *Ashby and Sammis*, 1990]. This means that propagation stops if no further stress is applied. For this reason, several microfractures are able to develop independently. Processes controlling fracture growth and coalescence will affect the final fracture pattern.

At high strain rates, several additional processes begin to interfere with the quasi-static processes described above.

1. An additional kinetic energy term cannot be neglected and must be taken into account for energy balance considerations [*Grady*, 1982].

2. The characteristic time for stress waves to propagate between fractures is not negligible compared to the characteristic time of propagation of a single fracture (Figure 4.10) [*Denoual and Hild*, 2000; *Hild et al.*, 2003].

3. Dynamic effects alter the way a single fracture propagates [*Freund*, 1990; *Bhat et al.*, 2012].

These additional processes will change the interaction between individual fractures, explaining the more intense fragmentation, and increase in strength that is observed for dynamic loading.

4.4.2. Models Constraining the Decrease in Grain Size with Increasing Strain Rate

Dynamic fracture damage is characterized by fragmentation leading to an intense reduction in grain size, which can be explained by several theories. A first breakthrough came with the energy consideration of *Grady* [1982]. He showed that fragmentation releases kinetic energy in a sufficient quantity to sustain fracture energy production. Indeed, the kinetic energy $U_K = \int_V \frac{1}{2}\rho(\tau)v(\tau)^2 d\tau$ is dependent on the particle velocity v of each particle τ constituting a volume V of mass density ρ. This velocity scales as the grain characteristic radius (R) multiplied by strain rate $\dot{\varepsilon}$, so that kinetic energy becomes $U_K \propto R^5\dot{\varepsilon}^2$. During fragmentation into N smaller spherical fragments of radii $S = \frac{R}{\sqrt[3]{N}}$, the kinetic energy decreases into $U_K = NU_{K,s} = \frac{1}{N^{2/3}}U_{K,R}$. This released kinetic energy is converted into new surface energy. If all kinetic energy ($U_K = NU_{K,s} \propto Ns^5\dot{\varepsilon}^2$) is converted into surface energy ($U_S \propto Ns^2$), the characteristic fragment size s would scale as $s \propto \dot{\varepsilon}^{-2/3}$. In a log-log diagram, giving characteristic fragment size versus strain rate, Grady's model would

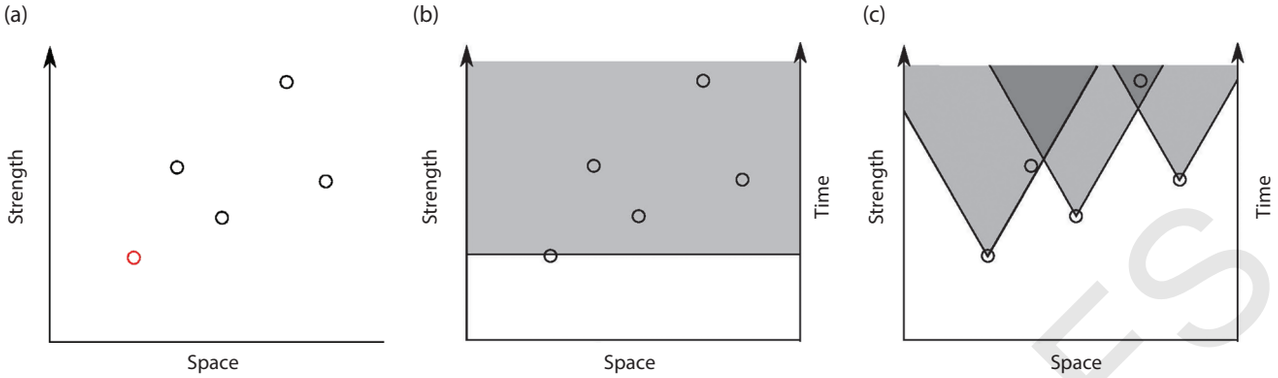

Figure 4.10 1D model for flaw propagation and interaction. (a) Preexisting flaws are scattered in space, with different strengths. As the stress increases, the weakest flaw fails. In case of a slow strain-loading rate (b), this flaw will propagate instantaneously compared to the strain rate. The sample will fail on this flaw only. (c) In case of fast loading, the stress relaxation waves will travel at finite speed. More flaws will be able to propagate, leading to a more fragmented final state. Sources: *Hild et al.* [2003], *Doan and D'Hour* [2012].

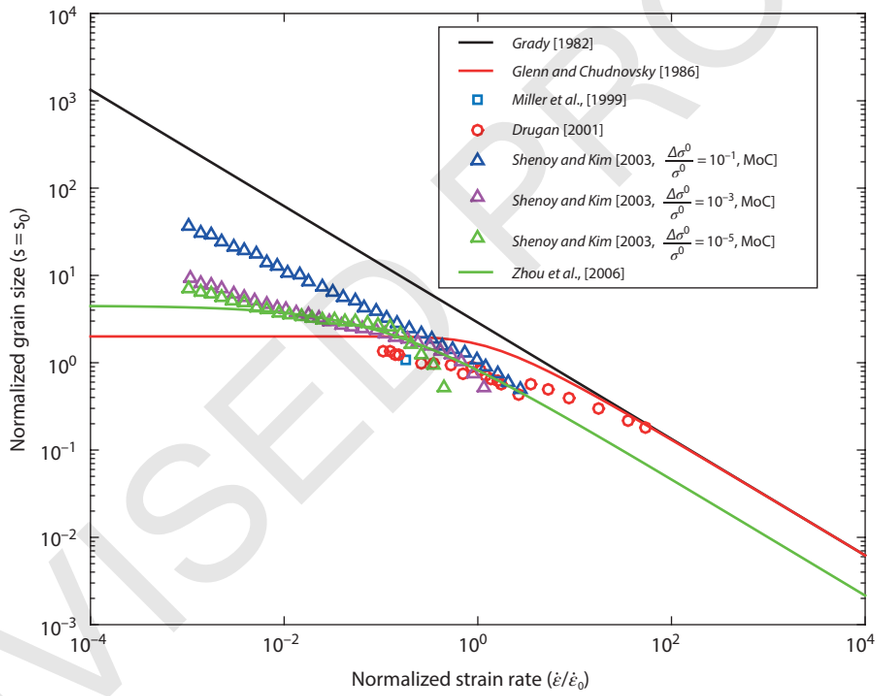

Figure 4.11 Theoretical fragment size versus strain rate predicted by several authors for an expanding 1D bar undergoing dynamic fragmentation. *Grady* [1982] and *Glenn and Chudnovsky* [1986] derive average grain size for homogeneous media using the energy balance. *Miller et al.* [1999] use a finite element method, with a cohesive law. The model is recomputed using a semianalytical model based on the dynamic instability analysis by *Drugan* [2001]. Disorder effects are taken into account by *Shenoy and Kim* [2003], who assume flaws with variable strength σ_0. Their model is still semi-analytical with the method of characteristics (MoC) applied on cohesive elements. Multiple reflection waves are taken into account by *Zhou et al.* [2006], resulting in a smaller grain size. In all models, fragment size becomes considerably smaller when the strain rate is above a threshold strain rate $\dot{\varepsilon}_0$.

correspond to a straight line (Figure 4.11). Such a release of kinetic energy has been considered to be the cause of the spectacular reduction in friction in catastrophic landslides [*Davies et al.*, 2006] and is also assumed to operate in the formation of fault gouges [*Davies et al.*, 2012].

Glenn and Chudnovsky [1986] refined this model by adding elastic energy in the energy balance. Contrary to kinetic energy, elastic energy is insensitive to strain rate and kinetic energy is negligible compared to elastic energy at low strain rate. Using the reformulation by *Zhou et al.* [2006],

the characteristic fragment size at low strain rate is shown to scale as

$$s_0 \propto \frac{EG_c}{\sigma_c^2}. \tag{4.8}$$

Fragment size increases with the critical energy release rate G_c and elastic moduli but decreases with the flaw nucleation threshold σ_c and remains independent of strain rate (Figure 4.11). Note that the parameter G_c bundles fracture energy per se and other plastic and frictional processes, and is often poorly known. As it estimates the energy required to create a new fracture area, it is sometimes abusively named fracture energy. It is related to the critical intensity factor K_c through $G_c = \alpha \frac{K_c^2}{E}$, where α depends on the loading condition (e.g., plane strain or plane stress). At high strain rate, kinetic energy dominates over elastic energy and Grady's law is restored (Figure 4.11). The transition between the two regimes takes place at the strain rate threshold:

$$\dot{\varepsilon}_0 = \frac{c_d \sigma_c^3}{E^2 G_c}. \tag{4.9}$$

The energy balance model is valid in case of equilibrium fragmentation, meaning that failure occurs as soon as a theoretical energy criterion is achieved [*Grady*, 2009]. However, it tends to overestimate grain size for nonequilibrium fragmentation, when there is a delay in failure [*Miller et al.*, 1999]. The reason for this is that during the additional time necessary for failure, new flaws can nucleate, propagate, and interact through stress waves.

These interactions between flaws become complex and numerical simulations are needed in order to model the change in fragment size with strain rate. The computations include cohesive elements between classical elastic elements. Cohesive elements are interface elements with edges that initially overlap. They can transmit forces F that depend on the displacement δ of the edge of the cohesive elements (Figure 4.12). A cohesive law linking F to δ is based on the physics of the individual failure process and must be established before performing the numerical simulations. Two such laws are commonly used: (1) *Camacho and Ortiz* [1996] introduced a linear weakening law that accounts for the finite propagation of individual fractures (Figure 4.12b). The area under the curve is related to the fracture energy G_C. (2) The law proposed by *Miller et al.* [1999] is (Figure 4.12c) $F = F_c \frac{\delta}{\delta_0} e^{-1\frac{\delta}{\delta_0}}$.

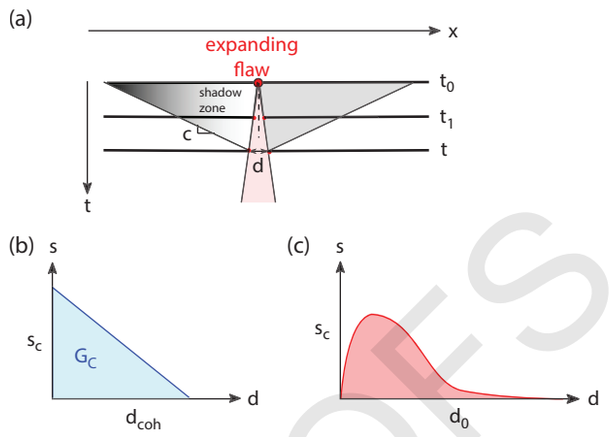

Figure 4.12 Cohesive element model introduced in numerical fragmentation models to demonstrate progressive failure of flaws [*Camacho and Ortiz*, 1996]. (a) In the 1D configuration, cohesive elements are implemented as two node elements whose displacement δ varies with time. During decohesion, healing waves are also released by the activated flaw. (b) With increasing displacement, flaws are less cohesive and sustain a smaller and smaller stress σ. The area under the curve is the fracture energy G_C. (c) Alternative cohesion model taking into account both activation and decohesion of the initial flaw.

When performing the numerical simulations, the problem regarding interactions between flaws is often reduced to the fragmentation of a dilating 1D bar. This is a geometry that is simple enough to focus on the effect of each individual process. Thanks to the increase in computational power of the last decades, it has now become possible to investigate a wide range of strain rates. *Drugan* [2001] first extended the model of *Miller et al.* [1999] by introducing a semianalytical model on a regular lattice of flaws. His simulations over three orders of strain rate magnitude confirmed the lower grain size compared to energy balance predictions, but they remained scattered (Figure 4.11). Using the simpler linear decay law of *Camacho and Ortiz* [1996], *Zhou et al.* [2006] were able to span eight orders of strain rate magnitude and found that their results would collapse on a single master law:

$$s = 4.5 \times \frac{s_0}{1 + 4.5 \times \left(\frac{\dot{\varepsilon}}{\dot{\varepsilon}_0}\right)^{2/3}} \tag{4.10}$$

where the characteristic grain size s_0 and the transition strain rate $\dot{\varepsilon}_0$ are the same as for *Glenn and Chudnovsky* [1986].

Stochastic effects have also been taken into account. *Shenoy and Kim* [2003] used the law by *Miller et al.* [1999] to estimate the effect of a heterogeneity $\Delta\sigma_c$ at a flaw

nucleation threshold σ_c. They found that greater variability would induce greater grain size, because the weaker flaws will reduce the stress around them while they extend, effectively inhibiting further fragmentation by shadowing other potentially nucleating flaws with a higher strength (Figure 4.10). *Levy and Molinari* [2010] went further by testing several statistical strength distributions. They found that, after being normalized by an adequate interaction parameter, the characteristic fragment size distribution would collapse on the law of *Zhou et al*. [2006]. However, their model does not include any time delay in nucleation, so that their final grain size is smaller than that found by *Shenoy and Kim* [2003].

Figure 4.11 summarizes the results of the studies briefly discussed above. In spite of their increasing complexity, these numerical models tend to follow Grady's scaling law at higher strain rates. They also show that fragment size diminishes beyond a strain rate threshold, as suggested by the dynamic loading experiments. The applicability of the grain size studies is, however, limited by poor knowledge of the actual flaw distribution in strength and space. Moreover, partial opening of fractures leads to difficulties with converting the newly created fracture area into a corresponding grain size distribution. Discussing strain rate effect on material strength rather than grain size is an alternative to determining a critical strain rate threshold.

4.4.3. Models Constraining the Increase in Strength with Increasing Strain Rate

The strength of a material can be modeled by reproducing the strain-stress curve, from which the peak stress acting on the sample during loading can be determined. A very simple example is the weakest link hypothesis, for which no fracture is activated (and the sample stays perfectly elastic) until the weakest flaw fails and instantaneously extends throughout the sample. In this extreme case of a brittle material, a fully analytical statistical strength law, the Weibull law [*Weibull*, 1939], can be derived, as long as the strength statistics of individual fractures are known (or equivalently, fracture length for Linear Elastic Fracture Mechanics).

Contrary to the discussion on fragment grain size, strength reflects the strain localization process that is initiated on the weakest flaws. Hence, if a uniform strength distribution is assumed for the sample flaws, this would greatly overestimate the sample strength. Discussion on sample strength is related to statistical approaches. The approach can stay fully stochastic so that the complexity of modern statistical physics (for example, percolation process, power laws in acoustic emissions, and phase transition modeling with increased correlation lengths [*Alava et al.*, 2006]) is maintained. However, this requires extensive numerical computational power.

A much easier approach is to assume that fractures remain at a moderate size all the time, so that at an intermediate scale (the mesoscopic scale) damage can be characterized by a local parameter. Usually, damage is described through a scalar parameter D that describes the diminution in elastic modulus: $E = E(1 - D)$. The parameter D lies between 0 (undamaged sample) and 1 (fully failed sample), so that an increasing amount of damage will induce strain softening and a diminution in strength. The same scheme can also be applied around an individual fracture to account for stress screening induced by the surrounding damage to implement self-consistent multiscale modeling of wing crack propagation [*Paliwal and Ramesh*, 2008; *Bhat et al.*, 2012].

When multiple fractures develop, several questions arise: (1) How do the fracture statistics change in space and in length, and (2) how does this fracturing process affect the (macroscopic) stress-strain relationship?

Hild and coworkers [*Denoual and Hild*, 2000, 2002; *Hild et al.*, 2003; *Forquin and Hild*, 2010] tried to answer these questions by focusing on the change in activated fractures. They assumed a uniform distribution in space and a power law distribution in fracture strengths. The weakest flaws are activated first, but by the time they start to propagate through the sample, other cracks are activated (Figure 4.10). *Hild et al*. [2003] developed a statistical law that describes the number of fractures activated over time, which is controlled by the initial power law statistics in fracture length. The number of activated flaws saturates to a number that is lower than the number of initial flaws but is much higher than the single fracture that the Weibull model would have predicted for quasi-static loading. The number of activated fractures is converted into an effective damage parameter to acquire a full macroscopic stress-strain curve at constant stress rate $\dot{\sigma}$. From such an analytical solution it follows that peak strength scales as $\sigma_{c,dyn} \propto \left[\frac{K_c^m}{\lambda_0}\right]^{\frac{1}{m+n}} \frac{n}{\dot{\sigma}^{m+n}}$, where K_c is the fracture toughness and λ_0 is the initial density of the preexisting fracture. Strength increases with stress rate according to a power law that depends on the dimensionality of the problem ($n = 1$ for an expanding bar, $n = 3$ for an expanding sphere). Statistics in fracture length are included through the Weibull shape parameter m (smaller fractures are more preeminent at larger m values, yielding a smaller variability in sample strength). The scatter in sample strength at higher loading rate is reduced compared to quasi-static loading. The intersection between the quasi-static weakest link regime and the dynamic fragmentation regime defines a characteristic stress rate (Figure 4.13a) that scales as

$$\dot{\sigma}_c \propto \lambda_0^{-\frac{1}{m}} \Omega_0^{\frac{1}{n}} V^{-\frac{m+n}{mn}}. \tag{4.11}$$

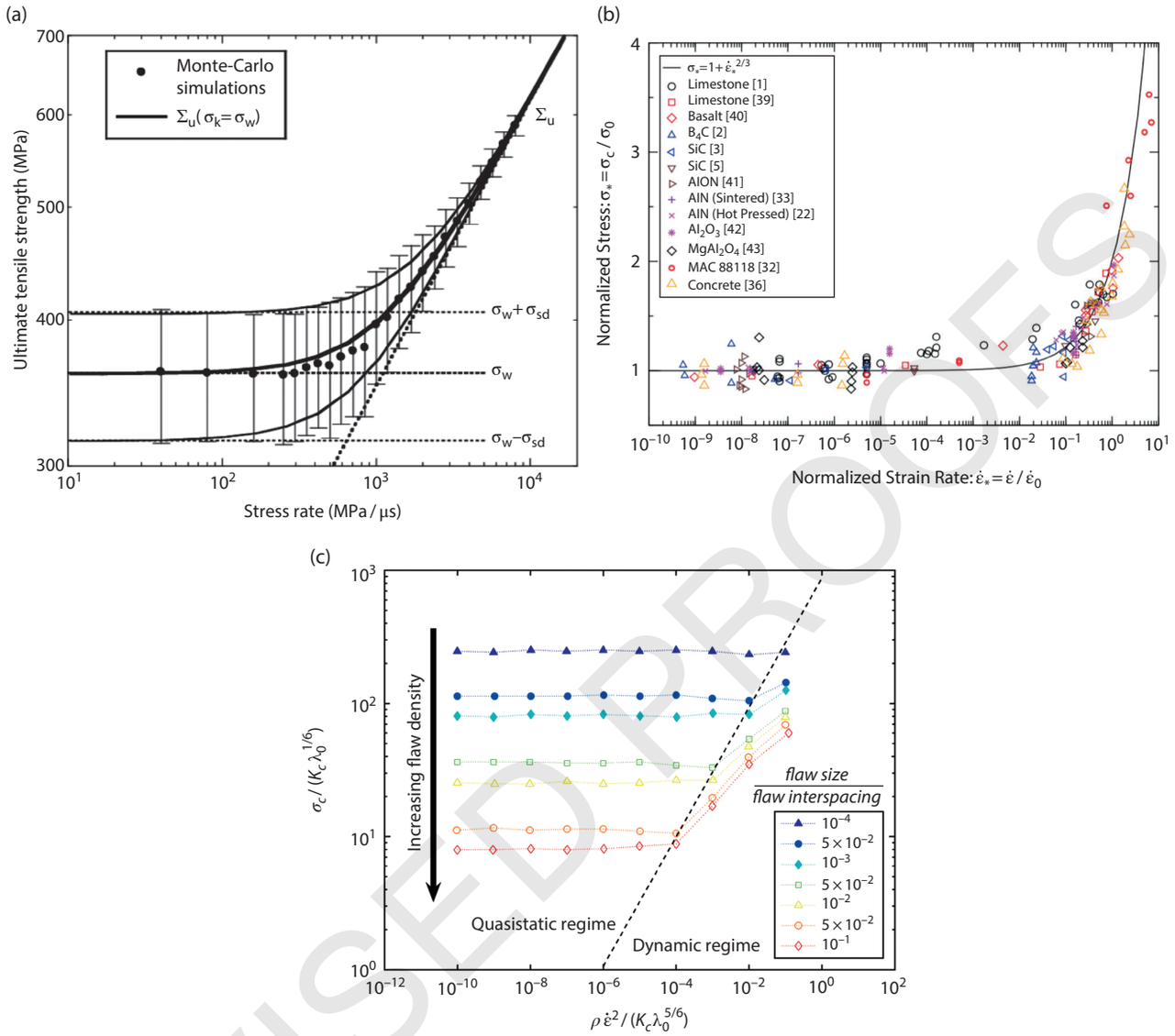

Figure 4.13 Several models showing a sudden increase in strength with strain rate. Here, the focus is placed on three models that predict a dependence of the critical strain rate on the initial microstructural properties of the sample. (a) 1D model of expanding flaws [*Hild et al.,* 2003]. (b) Systematic study of the 2D model of *Paliwal and Ramesh* [2008]. Graph from *Kimberley et al.* [2013] (c) 3D study by *Holland and McMeeking* [2015] specifically focusing on the effect of flaw density.

The threshold is therefore strongly dependent on the initial microstructure of the material, since the initial size of the shadow zone Ω_0 and the initial fracture size increase the threshold and the flaw density λ_0 decreases it. The threshold is also reduced for a larger volume V of the sample.

Since the analytical development of *Hild et al.* [2003], several micromechanical numerical models have been developed to describe high strain rate loading, especially in compression [*Paliwal and Ramesh*, 2008; *Deshpande and Evans*, 2008; *Bhat et al.*, 2012]. They assume that flaws are wing cracks developing from the edges of pre-existing favorably oriented cracks [*Ashby and Sammis*, 1990]. Here, all flaws are assumed to have the same size so differences in activation stress are not taken into account. These models introduce elasto-dynamic effects affecting propagation of individual fractures. Mean field theory is used to model stress evolution at the sample scale [*Paliwal and Ramesh*, 2008; *Deshpande and Evans*, 2008], meaning that each flaw is surrounded by the same stress and can be screened by the accumulated damage to account for weakening. In this way, a peak stress can be

derived [*Paliwal and Ramesh*, 2008]. *Deshpande and Evans* [2008] developed this into a 3D model of wing crack development. The 2D model of *Bhat et al.* [2012] is more refined in its formulation of elasto-dynamic effects, with rigorous expressions of the dynamic stress intensity factor and taking into account the increase in dynamic fracture toughness with loading rate.

The model of *Paliwal and Ramesh* [2008] is popular in the mechanical engineering community since it is less computationally demanding than models that require full implementation of cohesive elements [e.g. *Kraft et al.*, 2008]. Hence, it has been used extensively to perform sensitivity studies [*Graham-Brady*, 2010; *Kimberley et al.*, 2013]. *Kimberley et al*. [2013] systematically explored the space parameter and found that all their results collapse on a normalized equation (Figure 4.13b):

$$\frac{\sigma}{\sigma_0} = 1 + \left(\frac{\dot{\varepsilon}}{\dot{\varepsilon}_0} \right)^{2/3}, \tag{4.12}$$

where the characteristic stress σ_0 and the characteristic strain rate $\dot{\varepsilon}_0$ depend on three material parameters (E, K_C and c_d) and two microstructural parameters describing the preexisting damage (average fracture size s and average flaw density λ_0):

$$\sigma_0 \approx 2.4 \frac{K_c}{s\lambda_0^{1/4}} \tag{4.13}$$

$$\dot{\varepsilon}_0 \frac{\sigma_0 / E}{t_0} \approx 2.4 \frac{c_d K_c}{sE} \lambda_0^{1/4}. \tag{4.14}$$

Note that strain rate now increases with flaw density λ_0, contrary to the prediction of *Hild et al.* [2003]. This is due to the arbitrary choice of normalizing the critical strength $\varepsilon_0 = \sigma_0 / E$ by the time t_0, a parameter that gives the time of stress wave propagating between two flaws. This parameter, which scales at $\lambda_0^{-1/2}$, could have been replaced by another scaling parameter. However, since the master law of equation (4.12) bundles several parameters together, including a small exponent (1/4) for flaw density (equation 4.13), the actual sensitivity to flaw density is difficult to assess, especially given the scatter in experimental data from Figure 4.13b.

Holland and McMeeking [2015] systematically studied the effect of the various parameters cited by *Kimberley et al*. [2013] (equations 4.13 and 4.14). Instead of the 2D model of *Paliwal and Ramesh* [2008], they used the 3D microstructural wing crack model [*Deshpande and Evans*, 2008]. They found that the effect of the initial flaw density is complex (Figure 4.13c) because the normalizing strain rate of the master curve effectively increases with strain rate (in their normalization, characteristic strain rate scales as $\lambda_0^{5/6}$), but the actual effect of the initial flaw density is that it reduces the strength of the sample and, more importantly, reduces the strain rate threshold at which the strength of the sample increases.

Elasto-dynamics embodies how stress waves affect fracture opening ahead of the fracture tip. The dynamic stress intensity factor diminishes with crack propagation speed [*Freund*, 1990; *Bhat et al.*, 2012], even when neglecting the transient loading of the fracture tip. In contrast, dynamic experiments on notched samples show that fracture initiation toughness increases with loading rate [*Zhang and Zhao*, 2013a], resulting in a higher strength of a material. Both of these effects are introduced in the model by *Bhat et al.* [2012]. They introduce an empirical law linking the dynamic initiation toughness K_C^d to the dynamic stress intensity factor $\dot{K}$:

$$\frac{K_c^d}{K_c} = 1 + \frac{\dot{K}}{K_c} \times 2 \times 10^{-5} \left[\mathrm{s} \right], \tag{4.15}$$

where all quantities have been normalized to the static initiation toughness K_C. Also, when propagation commences, another empirical formulation describes the instant velocity of the crack tip and relates it to the dynamic stress intensity factor. Equation (4.15) introduces a dependence in strain rate from which *Bhat et al*. [2012] could model the increase in strength for a Dyonisus-Pentelicon marble at strain rates above $10^2\,\mathrm{s}^{-1}$. These results match the experimental results on this material. Despite the fact that the model lacks a thorough study of the effect of its individual parameters, it was easily extended to be applied to petrophysical issues, such as the sharp increase in permeability of pulverized rocks [*Morton et al.*, 2012; *Perol and Bhat*, 2013].

In this section, theoretical and numerical models all demonstrated that a strain rate threshold exists beyond which dynamic effects appear, leading to increasing strength and lower grain size, effectively inhibiting strain localization as previously observed in pulverized rocks. This threshold is partly controlled by the microstructural properties of the loaded solid. An intensively predamaged rock may be prone to further pulverization, which may affect the development of a very pulverized zone around an active fault [*Doan and D'Hour*, 2012].

4.5. DISCUSSION

4.5.1. Is Long-Distance Pulverization by Sub-Rayleigh Wave Speed Ruptures Possible?

Experimental results suggest that crystalline rocks can be pulverized near the surface (low confining pressure) when the strain rate during compressive loading

is ~200 s^{-1} (Figure 4.8b). Rupture models can be used to verify if such loading conditions are realistic during an earthquake rupture event, especially at the relatively large distances from the fault at which pulverized rocks are observed (Figures 4.2 and 4.4a). The most basic rupture model is derived from Linear Elastic Fracture Mechanics and analyzes the asymptotic stress field around a moving crack tip [*Freund*, 1990]. Here, an earthquake rupture tip will be treated as a mode II crack. Relative to the large size of a crustal-scale fault, distances up to hundreds of meters can be assumed to fall within the crack tip zone.

The following solution is valid for rupture velocities below the Rayleigh wave speed velocity and has the following form for the singular stress field [*Freund,* 1990: equation 4.3.24]:

$$\sigma_{ij} = \frac{K_{\mathrm{II}}(t)}{\sqrt{2\pi r}} \sum\nolimits_{ij}^{\mathrm{II}}(\theta,\upsilon), \tag{4.16}$$

where K_{II} is the elastic fracture intensity factor for a mode II fracture, r and θ are polar coordinates relative to the fracture tip, and v is the fracture tip velocity. The variable Σ gives the angular variation of each stress component:

$$\begin{aligned}
\sum\nolimits_{11}^{\mathrm{II}} &= -\frac{2\alpha_s}{D}\left\{\left(1+2\alpha_d^2-\alpha_s^2\right)\frac{\sin\left(\frac{1}{2}\theta_d\right)}{\sqrt{\gamma_d}} - \left(1+\alpha_s^2\right)\frac{\sin\left(\frac{1}{2}\theta_s\right)}{\sqrt{\gamma_s}}\right\} \\
\sum\nolimits_{12}^{\mathrm{II}} &= \frac{1}{D}\left\{4\alpha_d 2\alpha_s \frac{\cos\left(\frac{1}{2}\theta_d\right)}{\sqrt{\gamma_d}} - \left(1+\alpha_s^2\right)\frac{\cos\left(\frac{1}{2}\theta_s\right)}{\sqrt{\gamma_s}}\right\} \\
\sum\nolimits_{22}^{\mathrm{II}} &= \frac{2\alpha_s\left(1+\alpha_s^2\right)}{D}\left\{\frac{\sin\left(\frac{1}{2}\theta_d\right)}{\sqrt{\gamma_d}} - \frac{\sin\left(\frac{1}{2}\theta_s\right)}{\sqrt{\gamma_s}}\right\}.
\end{aligned} \tag{4.17}$$

D, α_d, and α_s are material-dependent variables and $\theta_{s/d}$ and $\gamma_{s/d}$ depend on polar coordinates:

$$\begin{aligned}
D &= 4\alpha_d\alpha_s - \left(1+\alpha_s^2\right)^2 \qquad \alpha_{s/d} = \sqrt{1-\left(\frac{\upsilon}{c_{s/d}}\right)^2} \\
\tan\theta_{s/d} &= \alpha_{s/d}\tan\theta \qquad\quad \gamma_{s/d} = \sqrt{1-\left(\frac{\upsilon\sin\theta}{c_{s/d}}\right)^2}.
\end{aligned} \tag{4.18}$$

Here, c_s and c_d are the S- and P-wave velocities, respectively. Note that D, called the Rayleigh function, vanishes when the rupture tip velocity approaches the Rayleigh wave speed.

The energy-term in equation (4.16) is K_{II}, which can be related to the energy release rate G:

$$G = \frac{1-\nu^2}{E} A_{\mathrm{II}}(\upsilon) K_{\mathrm{II}}^2 \quad A_{\mathrm{II}} = \frac{\upsilon^2\alpha_s}{(1-\nu)c_s^2 D}, \tag{4.19}$$

where A_{II} is a function of the rupture tip speed, E is Young's modulus and ν is Poisson's ratio. In turn, the energy release rate term can be adjusted to incorporate cohesive zone models so that the singularity of the stress field at the crack tip is eliminated [e.g., *Ida*, 1972; *Poliakov et al.*, 2001; *Rice et al.*, 2005]. Values of the energy release rate G (or substitute K_{II}-value) show considerable uncertainty because this parameter is difficult to define for earthquake ruptures and it changes with rupture velocity. In the literature, G values constrained for earthquakes range from 1×10^2 to 1×10^8 J/m^2 [*Kostrov and Das*, 1988; *Scholz*, 2002 and references therein; *Abercrombie and Rice*, 2005].

From equations (4.16) and (4.17), it follows that the maximum stress and strain decay with $r^{-0.5}$ and the strain rate decays with $r^{-1.5}$ with increasing distance from the rupture tip (Figure 4.14a). Computations using the above equations show that comminution with extreme grain size reduction associated with gouge formation very close to the fault plane (mm scale) are likely to occur during a sub-Rayleigh wave speed rupture [*Reches and Dewers*, 2005]. But, 100 m from the fault core, a strain rate of ~0.2 s^{-1} is insufficient to exceed the pulverization threshold [*Doan and Gary*, 2009]. Similar calculations fit the pulverization threshold of Carrara marble at 25 cm from the fault core [*Doan and Billi*, 2011]. For all these calculations, a K_{II} value of 30 MPa/m$^{0.5}$ was used.

Using a similar value for G as the studies above, a first-order approximation of the distance from the fault at which an intact igneous crystalline rock would be pulverized has been obtained. For this purpose, a pulverization strain rate threshold of 200 s^{-1} was taken. This yields a maximum pulverization distance of 6.2 and 26.2 cm for rupture velocities of respectively 0.8 and 0.91 times the shear wave speed (Figure 4.14b). Since the value used for G is in the lower range of values reported, an extreme value of 10^8 J/m^2 has also been used. This led to a significant increase in maximum distance to 3.19 m (Figure 4.14b).

According to several geophysical and petrophysical properties, elastic properties in the damage zone are altered and, for example, the Young's modulus may decrease by 50% [*Faulkner et al.*, 2006; *Rempe et al.*, 2013]. This initial damage has a twofold effect: (1) The Linear Elastic Fracture Mechanics rupture model indicates strain rates are higher at greater distance from the

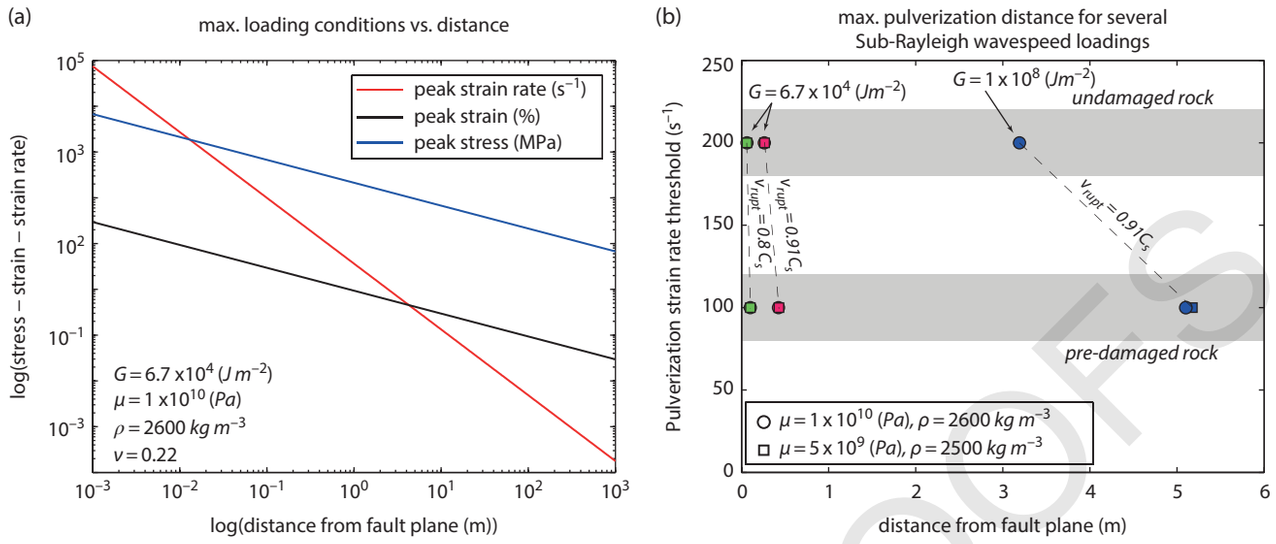

Figure 4.14 (a) Variation in the maximum stress (blue), strain (black), and strain rate (red) with distance from the fault according to a linear elastic fracture mechanics approach. The parameters used for this model are given in the bottom left corner. (b) Maximum distance of the pulverization boundary from the fault plane versus the preset pulverization threshold for several different rupture conditions and damage zone rocks. A 200 s^{-1} threshold for pristine rock and a 100 s^{-1} for damaged rock have been used. Furthermore, initial (circle) or reduced (square) mechanical properties are used. Two extremes for the energy-release-rate are applied as indicated, as well as different rupture velocities. *See electronic version for color representation.*

fault [*Doan and Billi*, 2011], and (2) initially damaged rocks show a pulverization strain rate threshold reduced by up to ~50% [*Doan and D'Hour*, 2012; *Aben et al.*, 2016] (Figure 4.8b). Effect 1 causes, for the most extreme case ($G = 10^8$ J/m^2), an increase of at most several centimeters in the pulverization boundary (Figure 4.14b). Effect 2, tested by reducing the pulverization strain rate threshold by 50% to 100 s^{-1}, causes an increase in distance of ~62% for all rupture models (Figure 4.14b). In terms of absolute distance, this causes the pulverization boundary to migrate 5.18 m for the most extreme case.

Systematic loading by sub-Rayleigh ruptures without preferred rupture direction would result in a symmetric damage zone geometry (Figure 4.15a), where a band of pulverized rocks close to the fault is followed by dynamically fractured rock. The pulverization boundary is several orders of magnitude closer to the fault than the damage zone boundary. At depth, the coseismic damage zone thins significantly because confinement increases the pulverization threshold [*Yuan et al.*, 2011]. It follows that strain rates induced by sub-Rayleigh wave speed ruptures are insufficient to exceed the pulverization threshold at distances from the fault where pulverized rocks have been observed (100 m or more). Nonetheless, near-fault pulverization during sub-Rayleigh wave speed ruptures is likely to occur and might be important for the formation of fault gouges [*Reches and Dewers*, 2005] and cataclasites.

4.5.2. Alternative Conditions for Coseismic Pulverization

Several alternatives that might solve the dilemma outlined above are discussed here. Two general aspects can be taken into account: the rock response to dynamic compressive loading under different conditions (e.g., saturated) that might reduce the pulverization threshold, and rupture mechanisms other than sub-Rayleigh wave speed ruptures possibly causing transient loading conditions that are sufficient for pulverization at great distance from the fault plane. Because these alternatives represent ongoing research and will require further experimental development, they are briefly discussed below.

4.5.2.1. Different Conditions During Loading: Pore Fluids

The established pulverization thresholds were determined under dry conditions, with and without confining pressure and with a variable amount of dynamically induced initial damage. However, the behavior of the pulverization threshold at other conditions has not yet been studied. One such condition that is likely to be found in nature is the presence of pore fluids. A high loading rate makes it hard for pore fluids to dissipate the stress, with the result that the rock is in an undrained state. According to the poroelastic theory, this would lead to a significant drop in effective failure strength. However, the pore fluid

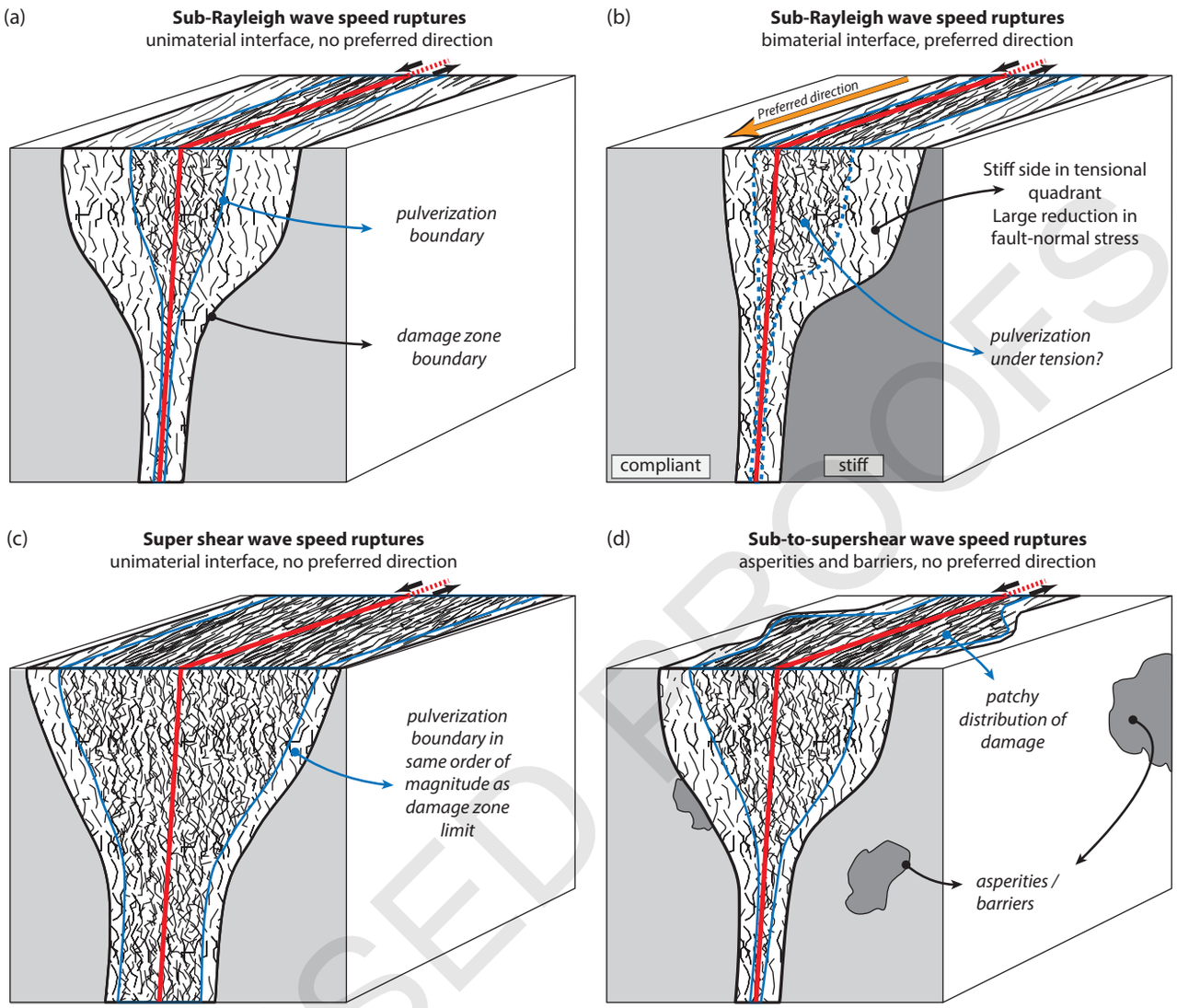

Figure 4.15 Conceptual damage zone geometries for several different rupture types. The red line indicates the fault plane with sense of movement (black arrows). The pulverized interval is bordered by a blue line, the damage zone boundary by black. (a) Geometry for systematic bilateral sub-Rayleigh rupture. The zone of pulverized rocks has a small width and thins quickly with depth. (b) Geometry for unilateral sub-Rayleigh ruptures with a preferred direction. The damage would be concentrated in the tensional quadrant, including pulverized rocks. (c) Bilateral supershear rupture geometry with a much larger zone of pulverized rocks within the same order of magnitude as the damage zone boundary. Pulverized rocks can extend to much greater depths relative to sub-Rayleigh ruptures. (d) Asperity- and barrier-controlled damage zone geometry that shows a much more patchy distribution of damage along the fault due to dynamic rupture velocities from sub- to supershear. *See electronic version for color representation*.

effect on the pulverization strain rate threshold is still unknown and might be subject to future research.

4.5.2.2. Sub-Rayleigh Wave Speed Loading Along a Bimaterial Interface

The loading conditions of a sub-Rayleigh rupture changes when the rupture occurs along a bimaterial interface instead of a single material interface. The difference in elastic wave velocities between two sides of the fault leads to the development of a so-called Weertman-pulse or wrinkle-like rupture [*Weertman*, 1980; *Andrews and Ben-Zion*, 1997; *Shi and Ben-zion*, 2006]. This means that a dilatant "wrinkle" originates in the more compliant material that reduces or increases the fault-normal stress,

depending on whether the more compliant side is in the compressional or tensional quadrant of the rupture. Consequently, the fault-normal stress is reduced or increased on the stiffer side as well. Rupture models [*Ben-Zion*, 2001; *Ben-Zion and Shi*, 2005; *Shi and Ben-zion*, 2006] show that a rupture in the direction of slip of the more compliant material is more stable and thus should be preferred. It therefore follows that the stiffer side of a fault should suffer more systematic extensional loading conditions.

Several authors relate the asymmetric distribution of pulverized rocks (that are more abundant on the stiffer side of the faults) to this systematic directional rupture property [*Dor et al.*, 2006a, 2008; *Mitchell et al.*, 2011] (Figure 4.15b). It follows that pulverized rocks must have formed during extensional loading. However, the limited data on tensile experiments do not reveal the same pervasive fracturing as that obtained under compressive dynamic loading. The contribution to the increase in strain rate is not yet fully understood, but the presence of Adams instabilities [*Adams*, 1995] during wrinkle-like ruptures can produce local short bursts in slip velocity [*Shi and Ben-zion*, 2006]. This might result in local high strain rate peaks and subsequent pulverization.

On another note, the reduction in fault-normal stress related to wrinkle-like ruptures does fit the loading conditions that are necessary for hydrofracturing by a transient stress drop. However, wrinkle-like ruptures have a depth limit of ~3 km [*Ben-Zion and Shi*, 2005] while pulverization by hydrofracturing needs sufficiently high fluid pressures that could be related to depth. Future research could focus on this promising mechanism.

4.5.2.3. Supershear Wave Speed Loading

Several authors suggest that supershear velocity ruptures are capable of pulverization-inducing loading conditions [*Doan and Gary*, 2009; *Yuan et al.*, 2011]. The stress field around a supersonic rupture tip that travels at constant velocity v ($c_s < v < c_d$) has two nearly decoupled contributions: the P- and S-wave speed stress fields, with c_s the shear wave velocity and c_d the P-wave velocity of the material, respectively. Three velocity-regimes exist for supershear ruptures: unstable between $c_s < v < \sqrt{2}c_s$, the unique value $v = \sqrt{2}c_s$, and the stable regime $\sqrt{2}c_s < v < c_d$. At $v = \sqrt{2}c_s$ the S-wave contribution to the rupture tip stress field disappears.

For the problem at hand, the most relevant modification to equation (4.16) to describe the P-wave contribution of the stress field is the replacement of the factor $r^{-0.5}$ by r^{-q} where q varies between 0 and 0.5, depending on the rupture velocity [*Freund*, 1990; *Dunham and Bhat*, 2008; *Mello et al.*, 2010]. This means that the P-wave contribution to the stress, strain, and strain-rate fields attenuates to a lesser extent with increasing distance from the rupture tip, except for the unique case of $v = \sqrt{2}c_s$, $q = 0.5$. Even more important, a Mach-cone forms at $q \neq 0.5$ since the radiated S-waves are slower than the rupture tip itself. Therefore, the S-wave loading contribution does not attenuate with distance [*Bernard and Baumont*, 2005], at least not up to a certain length scale related to the maximum depth of the seismogenic zone [*Dunham and Bhat*, 2008; *Ampuero*, 2014]. For the Mach-cone, equation (4.16) will include the Heaviside step function, which implies a theoretical infinite loading rate when the Mach-cone travels through the damage zone rocks.

The loading conditions during a supershear rupture with $v \neq \sqrt{2}c_s$ thus seem to be sufficient for pulverization at great distance from the fault. Even more, since the attenuation is nearly nonexistent, the pulverization boundary will be of the same order of magnitude as the damage zone boundary itself. This is also observed in the field (Figure 4.4a). Systematic bilateral ruptures would result in a symmetric damage zone with a large amount of pulverized rock (Figure 4.15c). Supershear ruptures have been observed on large faults with long straight sections only [*Bouchon et al.*, 2001, 2010; *Bouchon and Vallée*, 2003; *Dunham and Archuleta*, 2004], which matches the observation of pulverized rocks at such faults. A supershear rupture is more likely to develop in the direction of slip of the stiffer material in case of a bimaterial fault surface [*Weertman*, 2002; *Xia et al.*, 2005], resulting in an asymmetric damage distribution similar to that illustrated in Figure 4.15b, although it depends on whether more damage occurs in the tensile or compressive quadrant. However, the influence of asymmetric damage seems to eliminate this bimaterial effect [*Bhat et al.*, 2010].

A major remark for supershear as a damaging mechanism is that shear wave loading induces the high strain rates far from the fault. The experiments described in this review only focus on P-wave loading, and to our knowledge, no studies have focused on pulverization by shear stress waves. Also, S-wave Mach cones have zero divergence; thus, no volumetric deformation is expected. This marks a current gap in knowledge.

4.5.2.4. Heterogeneities Along the Rupture Interface

Heterogeneities along the fault plane, such as asperities and barriers, can cause acceleration of a sub-Rayleigh wave speed rupture toward supershear rupture speeds [*Dunham et al.*, 2003; *Dunham*, 2007; *Latour et al.*, 2013]. This mechanism requires less overall energy than the development of a stable supershear rupture. Such dynamic sub-to-super shear ruptures are likely to cause significant loading conditions far from the fault plane. However, pulverized rocks resulting from such ruptures would have a patchy distribution along the fault. These patches are geometrically related to the asperities or barriers (Figure 4.15d).

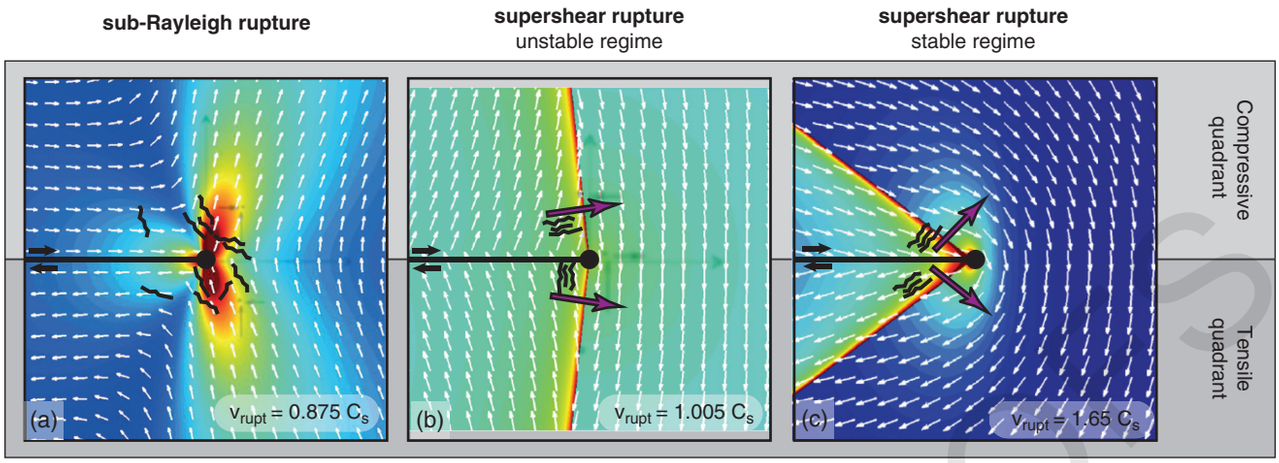

Figure 4.16 Particle motion fields for different rupture velocities (bottom right corner) in a homogeneous elastic material [adjusted from *Mello et al.,* 2010]. The purple arrows show the direction of maximum compressive or tensile loading rate, which is the gradient of the particle velocity field. Illustrative fractures indicate the expected fracture orientation, based on the maximum loading rate direction. The compressive and tensile quadrants are indicated on the right side. (a) Sub-Rayleigh wave speed rupture. (b), (c) Two supershear ruptures with unstable (b) and stable (c) rupture velocity. *See electronic version for color representation*.

4.5.3. Damage Anisotropy and Loading Conditions

Up to now, allowance has been made for maximum distance from the fault, depth, and asymmetric distribution of pulverized rock when analyzing the type of rupture necessary for pulverization. Another property now needs to be addressed: the damage anisotropy that has been observed in the field [*Rempe et al.*, 2013] as well as in laboratory experiments [*Aben et al.*, 2016]. If compressive SHPB experiments are projected to the setting of a fault zone to fit in with the anisotropy measured by *Rempe et al*. [2013], the transient compressive loading is parallel to the fault. Possibly, such anisotropy can be coupled to certain rupture modes. A qualitative illustration is given here of the approach that can be followed in analyzing fault rock anisotropy in combination with rupture models. Moreover, not all rupture mechanisms have been taken into consideration.

Although the upscaling of a 1D lab experiment to a complicated 3D radial stress field around a rupture tip is not straightforward, it is nonetheless worth discussing the direction of maximum extension or compression rate during some of the previously discussed rupture types in relation to damage anisotropy (Figure 4.16, adjusted from *Mello et al.* [2010]). Note that the direction of maximum stress is not necessarily the same as the direction of maximum loading rate. The effect of such decoupling (in the experiments both directions are similar) on damage anisotropy seems to be an open question. Besides, the maximum principal stress direction can vary from case to case because the far-field stress needs to be taken into account. This is not the case for the loading rate: the tectonic loading rates are negligible with respect to coseismic transient loading rates. Figure 4.16 shows particle velocities, with the maximum gradient of the particle velocities being indicative of the direction of the maximum loading rate.

The direction of maximum loading rate rotates during a sub-Rayleigh wave speed rupture from fault (sub-)parallel toward (sub-)perpendicular (up to 110°) when the stress field passes by a certain static point along the fault. The rotation thus occurs when stress is highest. This type of rupture is not therefore subject to unidirectional loading, making it hard to infer a clear anisotropy (Figure 4.16a). The S-wave Mach cones of unstable and stable supershear ruptures do have a unidirectional loading rate direction: an unstable supershear rupture has a maximum loading rate subparallel to the fault (Figure 4.16b). In the stable supershear regime the maximum loading rate is oriented at a higher angle to the fault (Figure 4.16c), although in both cases the angle changes with rupture speed. At $v = \sqrt{2}c_s$ the S-wave contribution disappears and coseismic damage will be more or less similar to the Sub-Rayleigh wave speed case.

Regardless of the orientation, fracture damage anisotropy can be expected to develop by the unilateral directed loading rate during supershear rupture (Figure 4.16b, c). This mechanism has been used to explain the formation of large cracks parallel to the fault during the 2001 Kunlun earthquake [*Bhat et al.*, 2007].

4.5.4. Other Implications for Fault Zones

Pulverization and coseismic damage are energy sinks that need to be taken into account for earthquake energy budgets. Seismic signals from pulverization-inducing earthquakes are different from the seismic signal predicted by an elastic model because pulverized rocks lose nearly all cohesion (Figure 4.9a). The stress amplitude of the wave is also significantly reduced. Such properties, observed in laboratory experiments, could provide a link to seismological observations of a major earthquake.

Pulverized rocks have different petrophysical and hydrological properties compared to nonpulverized damage zone rocks. Due to the contrast, post- and interseismic healing and sealing rates might differ spatially. For instance, *Richard et al*. [2014] showed that zones of microfracturing (i.e., pulverization) will heal faster than zones with only macroscopic fractures. This would result in a heterogeneous redistribution of strength in the damage zone during the interseismic phase. However, the reduced permeability of pulverized rocks may delay the transport of the precipitation product, or the increased surface area of pulverized rocks could increase the creep processes related to pressure solution. On a longer timescale this might result in differentiation of pulverized rocks from the rest of the damage zone in both mechanical and mineralogical terms. Possibly, such a differentiation becomes important for the formation of fault rocks that are prone to permanent creep.

4.6. PERSPECTIVES AND CONCLUSION

Pulverized rocks have mainly been observed in crystalline and cohesive granular rocks such as granitic rocks and limestones or dolostones, with the exception of sandstone. Also, pulverization is observed mostly near the surface along major strike-slip faults and is a shallow crustal feature (<10 km depth). The classic field definition of pulverization holds true only for igneous crystalline rocks and is ambiguous for limestones, dolostones, and sandstones. More experimental work is necessary to determine the nature of pulverization in these lithologies so that, with the help of dynamic fracture mechanics models, a more generalized definition can be developed.

Dynamic experiments in compression show that crystalline rocks can be pulverized under strain rates that fall well within the fracture kinetics controlled damage field. Pulverization in igneous crystalline rocks is revealed as a sharp threshold in strain rate. Whether other lithologies hold such a similar behavior remains to be investigated. Experimental studies show that the pulverization threshold decreases by initial damage or successive milder strain rate loadings but that it increases with confining pressure. The change in pulverization threshold during other conditions, such as saturation, should be subject to future research.

An attempt has been made to link field observations with the experimentally determined loading conditions necessary for pulverization. For this purpose, a simple sub-Rayleigh wave speed rupture model has been used. This shows that this type of rupture is not capable of exceeding the pulverization threshold for rocks located far from the fault (of the order of 100 m), although it can pulverize near-fault rocks. A qualitative discussion regarding the loading conditions of other types of ruptures suggests that supershear ruptures would be capable of pulverization at these long distances from the fault, although shear stress wave loading by supershear Mach cones has not yet been studied in laboratory experiments, and the question of whether S-waves can pulverize rocks remains open to discussion for the time being.

The issue of damage asymmetry across the fault plane, which has been observed for several fault systems, has not yet been solved. Either supershear ruptures or wrinkle-like ruptures could develop a unilateral propagation preference, or the lithology on the opposite side of the fault reacts differently to dynamic loading conditions. A better understanding of the rock response to dynamic tensile loading must also be developed, since these loading conditions contribute 50% of an earthquake rupture. Another pulverization mechanism, hydrofracturing by a transient stress drop, might be a promising alternative to compressive dynamic loading.

This review has outlined the link between field observations and experimental work regarding pulverized rocks. The potential constraints that these experiments can give on the rupture mechanics of large faults is of great significance, and therefore experimental research on pulverized rocks and coseismic damage will be of ongoing interest to the fault mechanics community. Finally, the specific stress waves observed in laboratory pulverization experiments are different from those where rocks are fractured only. This difference, seen in the laboratory, could also be looked for on seismograms of natural earthquakes and therefore extend our understanding of strain dissipation during major earthquakes.

ACKNOWLEDGMENTS

The authors would like to thank Anne-Marie Boullier for her helpful comments on the field section and her expertise on the Nojima fault in particular. The authors also thank Renaud Toussaint for the high speed camera acquisition. FMA was funded by the European Union's Seventh Framework Programme for research, technological development, and demonstration under grant agreement no. 316889 (ITN FlowTrans).

Table 4.1 List of symbols.

A	Surface area
A_B, A_S	(bar, sample)
c_d	P wave velocity (velocity of dilatational stress wave)
c_s	S wave velocity (velocity of shear stress wave)
D	Fractal dimension (section 1)
D	Damage parameter (section 4)
D	Rayleigh function (section 5)
δ	Displacement of cohesive elements (section 4)
E	Young's modulus
ε	Strain
$\dot{\varepsilon}$	Strain rate
$\dot{\varepsilon}_0$	Characteristic strain rate (= threshold in strain rate for pulverization)
F	Force
F_I, F_R, F_T	(incident, reflected, transmitted)
G	Energy release rate
G_C	Critical energy release rate
K	Stress intensity factor at a crack tip
K_{II}	Stress intensity factor at a mode II crack tip
$\dot{K}$	Stress intensity factor rate (= time derivative of K)
K_C	Fracture toughness (= critical stress intensity factor)
K_c^d	Dynamic fracture toughness (= critical stress intensity factor)
L	Length of the sample
λ_0	Initial density of flaws in the solid
m	Shape parameter of Weibull function
n	Dimension of the model
N	Number of fragments
ν	Poisson's ratio
θ	Angle to the rupture plane (used in polar coordinates)
r	Distance from rupture tip (used in polar coordinates)
R	Grain size characteristic radius
ρ	Mass density
σ	Size of individual fragments after fragmentation (=radius for spherical fragments)
σ_0	Characteristic fragment size
σ	Stress
σ_C	Critical stress for activation of an individual flaw
Σ	Angular stress variation at the crack tip
τ	Particle (in the sense on continuum mechanics)
v	Particle velocity (section 3 and 4)/Rupture velocity (section 5)
U_K	Kinetic energy
V	Volume of the sample
Ω_0	Minimal size of the shadow zone around each propagating flaw

REFERENCES

Aben, F. M., M.-L. Doan, T. M. Mitchell, R. Toussaint, T. Reuschlé, M. Fondriest, J.-P. Gratier, and F. Renard (2016), Dynamic fracturing by successive coseismic loadings leads to pulverization in active fault zones, *J. Geophys. Res. Solid Earth*, *121*, 1–23, doi:10.1002/2015JB012542.

Abercrombie, R. E., and J. R. Rice (2005), Can observations of earthquake scaling constrain slip weakening?, *Geophys. J. Int.*, *162*(2), 406–424, doi:10.1111/j.1365-246X.2005.02579.x.

Adams, G. G. (1995), Self-excited oscillations of two elastic half-spaces sliding with a constant coefficient of friction, *J. Appl. Mech.*, *62*(4), 867–872, doi:10.1115/1.2896013.

Agosta, F., and A. Aydin (2006), Architecture and deformation mechanism of a basin-bounding normal fault in Mesozoic platform carbonates, central Italy, *J. Struct. Geol.*, *28*(8), 1445–1467, doi:10.1016/j.jsg.2006.04.006.

Alava, M. J., P. K. V. V. Nukala, and S. Zapperi (2006), Statistical models of fracture, *Adv. Phys.*, *55*(3-4), 349–476, doi:10.1080/00018730300741518.

Ampuero, J.-P. (2014), Physical limits on damaged fault zone thickness: The role of seismogenic depth, in *AGU Fall Meeting 2014*, San Francisco.

Andrews, D. J., and Y. Ben-Zion (1997), Wrinkle-like slip pulse on a fault between different materials, *J. Geophys. Res.*, *102*(B1), 553–571, doi:doi:10.1029/96JB02856.

Ashby, M. F., and C. G. Sammis (1990), The damage mechanics of brittle solids in compression, *Pure Appl. Geophys.*, *133*(3), 489–521.

Asprone, D., E. Cadoni, A. Prota, and G. Manfredi (2009), Dynamic behavior of a Mediterranean natural stone under tensile loading, *Int. J. Rock Mech. Min. Sci.*, *46*(3), 514–520, doi:10.1016/j.ijrmms.2008.09.010.

Ben-Zion, Y. (2001), Dynamic ruptures in recent models of earthquake faults, *J. Mech. Phys. Solids*, *49*(9), 2209–2244, doi:10.1016/S0022-5096(01)00036-9.

Ben-Zion, Y., and Z. Shi (2005), Dynamic rupture on a material interface with spontaneous generation of plastic strain in the bulk, *Earth Planet. Sci. Lett.*, *236*(1-2), 486–496, doi:10.1016/j.epsl.2005.03.025.

Bernard, P., and D. Baumont (2005), Shear Mach wave characterization for kinematic fault rupture models with constant supershear rupture velocity, *Geophys. J. Int.*, *162*(2), 431–447, doi:10.1111/j.1365-246X.2005.02611.x.

Bhat, H. S., R. L. Biegel, A. J. Rosakis, and C. G. Sammis (2010), The effect of asymmetric damage on dynamic shear rupture propagation II: With mismatch in bulk elasticity, *Tectonophysics*, *493*(3-4), 263–271, doi:10.1016/j.tecto.2010.03.020.

Bhat, H. S., R. Dmowska, G. C. P. King, Y. Klinger, and J. R. Rice (2007), Off-fault damage patterns due to supershear ruptures with application to the 2001 Mw 8.1 Kokoxili (Kunlun) Tibet earthquake, *J. Geophys. Res.*, *112*(B6), B06301, doi:10.1029/2006JB004425.

Bhat, H. S., A. J. Rosakis, and C. G. Sammis (2012), A micromechanics based constitutive model for brittle failure at high strain rates, *J. Appl. Mech.*, *79*, 031016.1–031016.12, doi:10.1115/1.4005897.

Bouchon, M., M.-P. Bouin, K. Hayrullah, M. Nafi Toksoz, M. Dietrich, and A. J. Rosakis (2001), How fast is rupture during an earthquake? New insights from the 1999 Turkey earthquakes, *Geophys. Res. Lett.*, *28*(14), 2723–2726.

Bouchon, M., H. Karabulut, M.-P. Bouin, J. Schmittbuhl, M. Vallée, R. Archuleta, S. Das, F. Renard, and D. Marsan (2010), Faulting characteristics of supershear earthquakes, *Tectonophysics*, *493*(3-4), 244–253, doi:10.1016/j.tecto.2010.06.011.

Bouchon, M., and M. Vallée (2003), Observation of long supershear rupture during the magnitude 8.1 Kunlunshan earthquake, *Science*, *301*(5634), 824–6, doi:10.1126/science.1086832.

Boullier, A.-M. (2011), Fault-zone geology: Lessons from drilling through the Nojima and Chelungpu faults, *Geol. Soc. London, Spec. Publ.*, *359*(1), 17–37, doi:10.1144/SP359.2.

Brune, J. N. (2001), Fault-normal dynamic unloading and loading: An explanation for "non-gouge" rock powder and lack of fault-parallel shear bands along the San Andreas fault, in *AGU Fall Meeting 2001*, San Francisco.

Bürgmann, R., D. D. Pollard, and S. J. Martel (1994), Slip distributions on faults: effects of stress gradients, inelastic deformation, heterogeneous host-rock stiffness, and fault interaction, *J. Struct. Geol.*, *16*(12), 1675–1690, doi:10.1016/0191-8141(94)90134-1.

Cadoni, E. (2010), Dynamic characterization of orthogneiss rock subjected to intermediate and high strain rates in tension, *Rock Mech. Rock Eng.*, *43*(6), 667–676, doi:10.1007/s00603-010-0101-x.

Camacho, G. T., and M. Ortiz (1996), Computational modelling of impact damage in brittle materials, *Int. J. Solids Struct.*, *33*(20-22), 2899–2938, doi:10.1016/0020-7683(95)00255-3.

Chen, W., and B. Song (2011), *Split Hopkinson (Kolsky) Bar. Design, Testing and Applications*, 1st ed., Springer, New York.

Crampin, S., and D. Booth (1985), Shear-wave polarizations near the North Anatolian Fault - II. Interpretation in terms of crack-induced anisotropy, *Geophys. J. R. Astron. Soc.*, *83*, 75–92, doi:10.1111/j.1365-246X.1985.tb05157.x.

Davies, E. D. H., and S. C. Hunter (1963), The dynamic compression testing of solids by the method of the Split Hopkinson Pressure Bar, *J. Mech. Phys. Solids*, *11*, 115–179.

Davies, T. R. H., M. J. Mcsaveney, and R. D. Beetham (2006), Rapid block glides : Slide-surface fragmentation in New Zealand's Waikaremoana landslide, *Q. J. Eng. Geol. Hydrogeol.*, *39*, 115–129.

Davies, T. R. H., M. J. McSaveney, and C. J. Boulton (2012), Elastic strain energy release from fragmenting grains: Effects on fault rupture, *J. Struct. Geol.*, *38*, 265–277, doi:10.1016/j.jsg.2011.11.004.

Denoual, C., and F. Hild (2000), A damage model for the dynamic fragmentation of brittle solids, *Comput. Methods Appl. Mech. Eng.*, *183*(3-4), 247–258, doi:10.1016/S0045-7825(99)00221-2.

Denoual, C., and F. Hild (2002), Dynamic fragmentation of brittle solids: A multi-scale model, *Eur. J. Mech.*, *21*, 105–120.

Deshpande, V. S., and A. G. Evans (2008), Inelastic deformation and energy dissipation in ceramics: A mechanism-based constitutive model, *J. Mech. Phys. Solids*, *56*(10), 3077–3100, doi:10.1016/j.jmps.2008.05.002.

Doan, M.-L., and A. Billi (2011), High strain rate damage of Carrara marble, *Geophys. Res. Lett.*, *38*(19), doi:10.1029/2011GL049169.

Doan, M.-L., and V. D'Hour (2012), Effect of initial damage on rock pulverization along faults, *J. Struct. Geol.*, *45*, 113–124, doi:10.1016/j.jsg.2012.05.006.

Doan, M.-L., and G. Gary (2009), Rock pulverization at high strain rate near the San Andreas fault, *Nat. Geosci.*, *2*(10), 709–712, doi:10.1038/ngeo640.

Dor, O., Y. Ben-Zion, T. K. Rockwell, and J. N. Brune (2006b), Pulverized rocks in the Mojave section of the San Andreas Fault Zone, *Earth Planet. Sci. Lett.*, *245*(3-4), 642–654, doi:10.1016/j.epsl.2006.03.034.

Dor, O., J. S. Chester, Y. Ben-Zion, J. N. Brune, and T. K. Rockwell (2009), Characterization of damage in sandstones along the Mojave section of the San Andreas fault: Implications for the shallow extent of damage generation, *Appl. Geophys.*, *166*, 1747–1773, doi:10.1007/s00024-009-0516-z.

Dor, O., T. K. Rockwell, and Y. Ben-Zion (2006a), Geological observations of damage asymmetry in the structure of the San Jacinto, San Andreas and Punchbowl faults in Southern California: A possible indicator for preferred rupture propagation direction, *Pure Appl. Geophys.*, *163*, 301–349, doi:10.1007/s00024-005-0023-9.

Dor, O., C. Yildirim, T. K. Rockwell, Y. Ben-Zion, Ö. Emre, M. Sisk, and T. Y. Duman (2008), Geological and geomorphologic asymmetry across the rupture zones of the 1943 and 1944 earthquakes on the North Anatolian fault: Possible signals for preferred earthquake propagation direction, *Geophys. J. Int.*, *173*(2), 483–504, doi:10.1111/j.1365-246X.2008.03709.x.

Drugan, W. J. (2001), Dynamic fragmentation of brittle materials: Analytical mechanics-based models, *J. Mech. Phys. Solids*, *49*(6), 1181–1208.

Dunham, E. M. (2007), Conditions governing the occurrence of supershear ruptures under slip-weakening friction, *J. Geophys. Res. Solid Earth*, *112*(7), 1–24, doi:10.1029/2006JB004717.

Dunham, E. M., and R. J. Archuleta (2004), Evidence for a supershear transient during the 2002 Denali fault earthquake, *Bull. Seismol. Soc. Am.*, *94*(6B), 256–268, doi:10.1785/0120040616.

Dunham, E. M., and H. S. Bhat (2008), Attenuation of radiated ground motion and stresses from three-dimensional supershear ruptures, *J. Geophys. Res.*, *113*(B8), B08319, doi:10.1029/2007JB005182.

Dunham, E. M., P. Favreau, and J. M. Carlson (2003), A supershear transition mechanism for cracks, *Science*, *299*(5612), 1557–1559, doi:10.1126/science.1080650.

Faulkner, D. R., T. M. Mitchell, D. Healy, and M. J. Heap (2006), Slip on "weak" faults by the rotation of regional stress in the fracture damage zone., *Nature*, *444*(7121), 922–5, doi:10.1038/nature05353.

Faulkner, D. R., T. M. Mitchell, E. Jensen, and J. Cembrano (2011), Scaling of fault damage zones with displacement and the implications for fault growth processes, *J. Geophys. Res.*, *116*(B5), B05403, doi:10.1029/2010JB007788.

Fondriest, M., S. Aretusini, G. Di Toro, and S. A. Smith (2015), Fracturing and rock pulverization along an exhumed seismogenic fault zone in dolostones: The Foiana fault zone (Southern Alps, Italy), *Tectonophysics*, doi:10.1016/j.tecto.2015.04.015. [online] Available from: http://linkinghub.elsevier.com/retrieve/pii/S0040195115002401.

Forquin, P., and F. Hild (2010), A probabilistic damage model of the dynamic fragmentation process in brittle materials, *Adv. Appl. Mech.*, *44*, 1–72.

Forrestal, M. J., T. W. Wright, and W. Chen (2007), The effect of radial inertia on brittle samples during the split Hopkinson pressure bar test, *Int. J. Impact Eng.*, *34*(3), 405–411, doi:10.1016/j.ijimpeng.2005.12.001.

Freund, L. B. (1990), *Dynamic Fracture Mechanics*, Cambridge University Press, Cambridge.

Gama, B. A., S. L. Lopatnikov, and J. W. Gillespie (2004), Hopkinson bar experimental technique: A critical review, *Appl. Mech. Rev.*, *57*(4), 223, doi:10.1115/1.1704626.

Glenn, L. A., and A. Chudnovsky (1986), Strain-energy effects on dynamics fragmentation, *J. Applied Physics*, *59*(4), 1379–1380.

Grady, D. E. (1982), Local inertial effects in dynamic fragmentation, *J. Appl. Phys.*, *53*(1), 322–425.

Grady, D. E. (1998), Shock-wave compression of brittle solids, *Mech. Mater.*, *29*(3-4), 181–203, doi:10.1016/S0167-6636(98)00015-5.

Grady, D. E. (2009), *Analysis of shock and high-rate data for ceramics: Equation of state properties and fragmentation in the ballistic environment* [technical report].

Grady, D. E., R. E. Hollenbach, K. W. Schuler, and J. F. Callender (1977), Strain rate dependence in dolomite inferred from impact and static compression studies, *J. Geophys. Res.*, *82*(8), 1325, doi:10.1029/JB082i008p01325.

Graff, K. F. (1991), *Wave Motion in Elastic Solids*, Dover, New York.

Graham-Brady, L. (2010), Statistical characterization of meso-scale uniaxial compressive strength in brittle materials with randomly occurring flaws, *Int. J. Solids Struct.*, *47*(18-19), 2398–2413, doi:10.1016/j.ijsolstr.2010.04.034.

Gratier, J.-P., F. Thouvenot, L. Jenatton, A. Tourette, M.-L. Doan, and F. Renard (2013a), Geological control of the partitioning between seismic and aseismic sliding behaviours in active faults: Evidence from the Western Alps, France, *Tectonophysics*, *600*, 226–242, doi:10.1016/j.tecto.2013.02.013.

Gratier, J.-P., D. K. Dysthe, and F. Renard (2013b), The role of pressure solution creep in the ductility of the Earth, *Adv. Geophys.*, *54*, 47–179, doi:10.1016/B978-0-12-380940-7.00002-0.

Gratier, J.-P., F. Renard, and B. Vial (2014), Postseismic pressure solution creep: Evidence and time-dependent change from dynamic indenting experiments, *J. Geophys. Res. Solid Earth*, *119*, 2764–2779, doi:10.1002/2013JB010768. Received.

Hild, F., P. Forquin, and A. R. Cordeiro da Silva (2003), Single and multiple fragmentation of brittle geomaterials, *Rev. française génie …*, *7*(7-8), 973–1002. [online] Available from: http://www.tandfonline.com/doi/abs/10.1080/12795119.2003.9692529 (Accessed 17 January 2014)

Holland, C. C., and R. M. McMeeking (2015), The influence of mechanical and microstructural properties on the rate-dependent fracture strength of ceramics in uniaxial compression, *Int. J. Impact Eng.*, *81*, 34–49, doi:10.1016/j.ijimpeng.2015.02.007.

Ida, Y. (1972), Cohesive force across the tip of a longitudinal-shear crack and Griffith's specific surface energy, *J. Geophys. Res.*, *77*(20), 3796, doi:10.1029/JB077i020p03796.

Keulen, N., R. Heilbronner, H. Stünitz, A.-M. Boullier, and H. Ito (2007), Grain size distributions of fault rocks: A comparison between experimentally and naturally deformed granitoids, *J. Struct. Geol.*, *29*(8), 1282–1300, doi:10.1016/j.jsg.2007.04.003.

Key, W. R. O., and R. A. Schultz (2011), Fault formation in porous sedimentary rocks at high strain rates: First results from the Upheaval Dome impact structure, Utah, USA, *Geol. Soc. Am. Bull.*, *123*(5-6), 1161–1170, doi:10.1130/B30087.1.

Kimberley, J., K. T. Ramesh, and N. P. Daphalapurkar (2013), A scaling law for the dynamic strength of brittle solids, *Acta Mater.*, *61*(9), 3509–3521, doi:10.1016/j.actamat.2013.02.045.

Kolsky, H. (1949), An investigation of the mechanical properties of materials at very high rates of loading, *Proc. Phys. Soc. Sect. B*, *62*(11), 676, doi:doi:10.1088/0370-1301/62/11/302.

Kostrov, B. V., and S. Das (1988), *Principles of Earthquake Source Mechanics*, Cambridge University Press, London.

Kraft, R. H., J.-F. Molinari, K. T. Ramesh, and D. H. Warner (2008), Computational micromechanics of dynamic compressive loading of a brittle polycrystalline material using a distribution of grain boundary properties, *J. Mech. Phys. Solids*, *56*(8), 2618–2641, doi:10.1016/j.jmps.2008.03.009.

Latour, S., C. Voisin, F. Renard, E. Larose, S. Catheline, and M. Campillo (2013), Effect of fault heterogeneity on rupture dynamics: An experimental approach using ultrafast ultrasonic imaging, *J. Geophys. Res. Solid Earth*, *118*(11), 5888–5902, doi:10.1002/2013JB010231.

Levy, S., and J. F. Molinari (2010), Dynamic fragmentation of ceramics, signature of defects and scaling of fragment sizes, *J. Mech. Phys. Solids*, *58*(1), 12–26, doi:10.1016/j.jmps.2009.09.002.

Li, X. B., T. S. Lok, and J. Zhao (2005), Dynamic characteristics of granite subjected to intermediate loading rate, *Rock Mech. Rock Eng.*, *38*(1), 21–39, doi:10.1007/s00603-004-0030-7.

Li, Y. G., J. E. Vidale, S. M. Day, D. D. Oglesby, and E. Cochran (2003), Postseismic fault healing on the rupture zone of the 1999 M 7.1 Hector Mine, California, earthquake, *Bull. Seismol. Soc. Am.*, *93*(2), 854–869, doi:10.1785/0120020131.

Lyakhovsky, V., and Y. Ben-Zion (2014), A continuum damage-breakage faulting model and solid-granular transitions, *Pure Appl. Geophys.*, doi:10.1007/s00024-014-0845-4.

Mello, M., H. S. Bhat, A. J. Rosakis, and H. Kanamori (2010), Identifying the unique ground motion signatures of supershear earthquakes: Theory and experiments, *Tectonophysics*, *493*(3-4), 297–326, doi:10.1016/j.tecto.2010.07.003.

Miller, O., L. B. Freund, and A. Needleman (1999), Modeling and simulation of dynamic fragmentation in brittle materials, *Int. J. Fract.*, *96*, 101–125, doi:10.1023/A:1018666317448.

Miller, S. A. (2013), The role of fluids in tectonic and earthquake processes, *Advances in Geophysics*, *54*, 1–46.

Mitchell, T. M., Y. Ben-Zion, and T. Shimamoto (2011), Pulverized fault rocks and damage asymmetry along the Arima-Takatsuki Tectonic Line, Japan, *Earth Planet. Sci. Lett.*, *308*(3-4), 284–297, doi:10.1016/j.epsl.2011.04.023.

Mitchell, T. M., A. Billi, S. A. Miller, D. Goldsby, C. H. Scholz, J. K. Gran, and J. Simons (2013), Dynamic pulverization by rapid decompression, in *AGU Fall Meeting 2013*, San Francisco.

Mitchell, T. M., and D. R. Faulkner (2009), The nature and origin of off-fault damage surrounding strike-slip fault zones with a wide range of displacements: A field study from the

Atacama fault system, northern Chile, *J. Struct. Geol.*, *31*(8), 802–816, doi:10.1016/j.jsg.2009.05.002.

Monzawa, N., and K. Otsuki (2003), Comminution and fluidization of granular fault materials: Implications for fault slip behavior, *Tectonophysics*, *367*(1-2), 127–143, doi:10.1016/S0040-1951(03)00133-1.

Morton, N., T. M. Mitchell, M.-L. Doan, G. Girty, T. K. Rockwell, and J. Renner (2012), Ultra-high permeability induced by seismic shockwaves near the San Jacinto fault, in *AGU Fall Meeting 2012*, San Francisco.

Muto, J., T. Nakatani, O. Nishikawa, and H. Nagahama (2015), Fractal particle size distribution of pulverized fault rocks as a function of distance from the fault core, *Geophys. Res. Lett.*, 1–9, doi:10.1002/2015GL064026.

Nemat-Nasser, S., and H. Horii (1982), Compression-induced nonplanar crack extension with application to splitting, exfoliation, and rockburst, *J. Geophys. Res.*, *87*(B8), 6805–6821, doi:10.1029/JB087iB08p06805.

Nemat-Nasser, S., J. B. Isaacs, and J. E. Starrett (1991), Hopkinson techniques for dynamic recovery experiments, *Proc. R. Soc. London, Ser. A*, *435*(1894), 371–391.

Paliwal, B., and K. T. Ramesh (2008), An interacting microcrack damage model for failure of brittle materials under compression, *J. Mech. Phys. Solids*, *56*(3), 896–923, doi:10.1016/j.jmps.2007.06.012.

Paterson, M. S., and T.-F. Wong (2005), *Experimental rock deformation: The brittle field*, Springer Verlag.

Perol, T., and H. S. Bhat (2013), Micromechanics based permeability evolution in brittle materials at high strain rates, *American Geophysical Union 2013*.

Poliakov, A. N. B., R. Dmowska, and J. R. Rice (2001), Dynamic shear rupture interactions with fault bends and off-axis secondary faulting, *J. Geophys. Res.*, *107*(B11), 1–48, doi:10.1029/2001JB000572.

Ravichandran, G., and G. Subhash (1994), Critical appraisal of limiting strain rates for compression testing of ceramics in a split Hopkinson pressure bar, *J. Am. Ceram. Soc.*, *77*(1), 263–267.

Reches, Z., and T. A. Dewers (2005), Gouge formation by dynamic pulverization during earthquake rupture, *Earth Planet. Sci. Lett.*, *235*(1-2), 361–374, doi:10.1016/j.epsl.2005.04.009.

Rempe, M., T. M. Mitchell, J. Renner, S. Nippress, Y. Ben-Zion, and T. K. Rockwell (2013), Damage and seismic velocity structure of pulverized rocks near the San Andreas Fault, *J. Geophys. Res. Solid Earth*, *118*(6), 2813–2831, doi:10.1002/jgrb.50184.

Rice, J. R., C. G. Sammis, and R. Parsons (2005), Off-fault secondary failure induced by a dynamic slip pulse, *Bull. Seismol. Soc. Am.*, *95*(1), 109–134, doi:10.1785/0120030166.

Richard, J., M.-L. Doan, J.-P. Gratier, and F. Renard (2014), Microstructures induced in porous limestone by dynamic loading, and fracture healing: An experimental approach, *Pure Appl. Geophys.*, doi:10.1007/s00024-014-0958-9. [online] Available from: http://link.springer.com/10.1007/s00024-014-0958-9.

Rockwell, T. K., M. Sisk, G. Girty, O. Dor, N. Wechsler, and Y. Ben-Zion (2009), Chemical and physical characteristics of pulverized tejon lookout granite adjacent to the San Andreas and garlock faults: Implications for earthquake physics, *Pure Appl. Geophys.*, *166*(10-11), 1725–1746, doi:10.1007/s00024-009-0514-1.

Rosakis, A. J., and G. Ravichandran (2000), Dynamic failure mechanics, *Int. J. Solids Struct.*, *37*(1-2), 331–348, doi:10.1016/S0020-7683(99)00097-9.

Sagy, A., and D. Korngreen (2012), Dynamic branched fractures in pulverized rocks from a deep borehole, *Geology*, *40*(9), 799–802, doi:10.1130/G33194.1.

Savage, H. M., and E. E. Brodsky (2011), Collateral damage: Evolution with displacement of fracture distribution and secondary fault strands in fault damage zones, *J. Geophys. Res. Solid Earth*, *116*(3), doi:10.1029/2010JB007665.

Scholz, C. H. (2002), *The Mechanics of Earthquakes and Faulting*, 2nd ed., Cambridge University Press, Cambridge.

Shenoy, V. B., and K.-S. Kim (2003), Disorder effects in dynamic fragmentation of brittle materials, *J. Mech. Phys. Solids*, *51*(11-12), 2023–2035, doi:10.1016/j.jmps.2003.09.010.

Shi, Z., and Y. Ben-zion (2006), Dynamic rupture on a bimaterial interface governed by slip-weakening friction, *Geophys. J. Int.*, *165*(2), 469–484, doi:10.1111/j.1365-246X.2006.02853.x.

Sibson, R. H. (1977), Fault rocks and fault mechanisms, *J. Geol. Soc. London.*, *133*(3), 191–213, doi:10.1144/gsjgs.133.3.0191.

Sibson, R. H. (1996), Structural permeability of fluid-driven fault-fracture meshes, *J. Struct. Geol.*, *18*(8), 1031–1042, doi:10.1016/0191-8141(96)00032-6.

Stünitz, H., N. Keulen, T. Hirose, and R. Heilbronner (2010), Grain size distribution and microstructures of experimentally sheared granitoid gouge at coseismic slip rates: Criteria to distinguish seismic and aseismic faults? *J. Struct. Geol.*, *32*(1), 59–69, doi:10.1016/j.jsg.2009.08.002.

Di Toro, G., D. L. Goldsby, and T. E. Tullis (2004), Friction falls towards zero in quartz rock as slip velocity approaches seismic rates., *Nature*, *427*(6973), 436–439, doi:10.1038/nature02249.

Wechsler, N., E. E. Allen, T. K. Rockwell, G. Girty, J. S. Chester, and Y. Ben-Zion (2011), Characterization of pulverized granitoids in a shallow core along the San Andreas fault, Littlerock, CA, *Geophys. J. Int.*, *186*(2), 401–417, doi:10.1111/j.1365-246X.2011.05059.x.

Weertman, J. (1980), Unstable slippage across a fault that separates elastic media of different elastic constants, *J. Geophys. Res.*, *85*(B3), 1455–1461, doi:doi:10.1029/JB085iB03p01455.

Weertman, J. (2002), Subsonic type earthquake dislocation moving at approximately sqrt(2)x shear wave velocity on interface between half spaces of slightly different elastic constants, *Geophys. Res. Lett.*, *29*(10), 10–13.

Weibull, W. (1939), A statistical theory of the strength of materials, *Ingeniörsvetenskapsakademiens Handl.*, *151*, 1–4.

Wilson, B., T. Dewers, Z. Reches, and J. N. Brune (2005), Particle size and energetics of gouge from earthquake rupture zones, *Geophys. Res. Lett.*, *434*, 749–752, doi:10.1029/2003GL019277.

Wong, T., R. H. C. Wong, K. T. Chau, and C. A. Tang (2006), Microcrack statistics, Weibull distribution and micromechanical modeling of compressive failure in rock, *Mech. Mater.*, *38*(7), 664–681, doi:10.1016/j.mechmat.2005.12.002.

Xia, K., M. H. B. Nasseri, B. Mohanty, F. Lu, R. Chen, and S. N. Luo (2008), Effects of microstructures on dynamic compression of Barre granite, *Int. J. Rock Mech. Min. Sci.*, *45*, 879–887, doi:10.1016/j.ijrmms.2007.09.013.

Xia, K., A. J. Rosakis, H. Kanamori, and J. R. Rice (2005), Laboratory earthquakes along inhomogeneous faults: Directionality and supershear, *Science*, *308*(5722), 681–684, doi:10.1126/science.1108193.

Xia, K., and W. Yao (2015), Dynamic rock tests using split Hopkinson (Kolsky) bar system: A review, *J. Rock Mech. Geotech. Eng.*, *7*(1), 27–59, doi:10.1016/j.jrmge.2014.07.008.

Yuan, F., V. Prakash, and T. Tullis (2011), Origin of pulverized rocks during earthquake fault rupture, *J. Geophys. Res.*, *116*(B6), B06309, doi:10.1029/2010JB007721.

Zhang, Q. B., and J. Zhao (2013), A review of dynamic experimental techniques and mechanical behaviour of rock materials, *Rock Mech. Rock Eng.*, doi:10.1007/s00603-013-0463-y.

Zhao, D., Z. Huang, N. Umino, A. Hasegawa, and H. Kanamori (2011), Structural heterogeneity in the megathrust zone and mechanism of the 2011 Tohoku-Oki earthquake (Mw 9.0), *Geophys. Res. Lett.*, *38*(17), 5–9, doi:10.1029/2011GL048408.

Zhou, F., J.-F. Molinari, and K. T. Ramesh (2006), Characteristic fragment size distributions in dynamic fragmentation, *Appl. Phys. Lett.*, *88*(26), 261918, doi:10.1063/1.2216892.

Zhao, H., and G. Gary (1996), On the use of SHPB techniques to determine the dynamic behavior of materials in the range of small strains, *Int. J. Solids Struct.*, *33*(23), 3363–3375.

Zöller, G., M. Holschneider, and Y. Ben-Zion (2005), The role of heterogeneities as a tuning parameter of earthquake dynamics, *Pure Appl. Geophys.*, *162*(6-7), 1027–1049, doi:10.1007/s00024-004-2660-9.